A Facet-Based Numerical Model for Simulating SAR Altimeter Echoes from Heterogeneous Sea Ice Surfaces

Jack C. Landy, Michel Tsamados, and Randall K. Scharien

***Abstract*— Cryosat-2 has provided measurements of pan-Arctic sea ice thickness since 2010 with unprecedented spatial coverage and frequency. However, it remains uncertain how the Ku-band radar interacts with the vast range of scatterers that can be present within the satellite footprint, including sea ice with varying physical properties and multi-scale roughness, snow cover, and leads. Here, we present a numerical model designed to simulate delay-Doppler SAR (Synthetic Aperture Radar) altimeter echoes from snow-covered sea ice, such as those detected by Cryosat-2. Backscattered echoes are simulated directly from triangular facet-based models of actual sea ice topography generated from Operation IceBridge Airborne Topographic Mapper (ATM) data, as well as virtual statistical models simulated artificially. We use these waveform simulations to investigate the sensitivity of SAR altimeter echoes to variations in satellite parameters (height, pitch, roll) and sea ice properties (physical properties, roughness, presence of water). We show that the conventional Gaussian assumption for sea ice surface roughness may be introducing significant error into the Cryosat-2 waveform retracking process. Compared to a more representative lognormal surface, an echo simulated from a Gaussian surface with rms roughness height of 0.2 m underestimates the ice freeboard by 5 cm – potentially underestimating sea ice thickness by around 50 cm. We present a set of 'ideal' waveform shape parameters simulated for sea ice and leads to inform existing waveform classification techniques. This model will ultimately be used to improve retrievals of key sea ice properties, including freeboard, surface roughness and snow depth, from SAR altimeter observations.**

***Index Terms*—Radar Altimetry; Synthetic Aperture Radar; Radar Scattering; Numerical Analysis; Modeling; Sea Ice; Snow.**

I. Introduction

THE Cryosat-2 Synthetic Aperture Interferometric Radar Altimeter (SIRAL) has proven an immensely successful tool for monitoring global ice and ocean properties. It has allowed us to estimate interannual ice sheet mass balance [1], the global marine gravity field [2], coastal & polar (i.e. ice-covered) ocean dynamic topography and geostrophic circulation [3, 4], and sea ice thickness [5, 6], with unprecedented spatial coverage, frequency and accuracy. Recent work has demonstrated that sea ice extent is closely tied to the inter-seasonal 'memory' of ice thickness [7], which means that sea ice models initialized with thickness observations can substantially improve the skill of ice extent forecasts [8, 9, 10]. However, improvements in forecasting clearly depend on the accuracy and uncertainty of the ice thickness observations used to initialize a model.

Synthetic aperture processing has reduced the sampling interval and size of the Cryosat-2 sensing footprint along the track of the satellite to only a few hundred meters, in comparison to conventional pulse-limited altimeters operating on kilometer scales [11]. This is crucial for discriminating between returns from sea ice and ocean, and accurately determining the ice surface elevation from which the radar wave is backscattered; the two essential prerequisites for measuring sea ice freeboard using altimetry. Yet uncertainties remain with both procedures [12]. Here, we develop a numerical model for simulating delay-Doppler SAR altimeter echoes backscattered from heterogenous snow-covered sea ice surfaces, designed to explore these uncertainties and ultimately improve sea ice property retrievals.

Radar altimeter echoes from the polar oceans have conventionally been classified into sea ice, lead or open water classes based on the shape of the backscattered waveforms. Ice and water have very different scattering characteristics at the Ku-band frequency commonly used by altimeters, meaning that classes can be separated using the width or 'peakiness' of waveforms [5], total backscattered power [13], and various other parameters [6]. However, the scattering properties of sea ice vary widely, depending on sea ice thermodynamics, surface roughness and properties of the overlying snow cover [14, 15]. Moreover, leads within the icepack commonly exist at a scale below the Cryosat-2 pulse-limited footprint (<1500 m), and often not at the nadir-point of the radar antenna, resulting in waveforms combining a heterogenous mix of scatterers. Off-

J.C.L. acknowledges support from the European Space Agency Living Planet Fellowship ESA/4000125582/18/I-NS 'Arctic-SummIT' and from the Natural Environment Research Council grant NE/R012849/1 'Diatom-ARCTIC'. M.T. acknowledges support from the European Space Agency snow project ESA/AO/1-8377/15/I-NB - 'STSE - Arctic+' and the SKIM Mission Science Study (SKIM-SciSoc) project ESA RFP 3-15456/18/NL/CT/gp. R.K.S. acknowledges support from a Natural Sciences and Engineering Research Council (NSERC) Discovery Grant (DG).

J. C. Landy is with the School of Geographical Sciences, University of Bristol, Bristol BS8 1SS, U.K. (e-mail: jack.landy@bristol.ac.uk).

M. Tsamados is with the Centre for Polar Observation and Modeling, University College London, London WC1E 6BT, U.K. (e-mail: m.tsamados@ucl.ac.uk).

R. K. Scharien is with the Department of Geography, University of Victoria, Victoria, B.C. V8W 2Y2, Canada (e-mail: randy@uvic.ca).

TABLE I
COMPARISON OF PHYSICAL MODELS FOR THE BACKSCATTERED SAR ALTIMETER ECHO

	CS2WfF [17]	SAMOSA+ [23, 27]	WINGHAM [28]	Here
Type*	Semi-analytical	Analytical	Semi-analytical	Numerical
Mode(s)	PL/SAR	SAR	PL/SAR/SARIn	PL/SAR
Roughness	Stochastic (Gaussian)	Stochastic (Gaussian)	Stochastic (Gaussian)	Deterministic
Target	Sea Ice & Leads	Sea Ice & Inland Water	Ocean & Ice Sheets	Snow, Sea Ice & Leads
Backscattering Properties	Approximated	Approximated	Modelled	Modelled
Scattering Mechanism Decomposition	No	No	No	Yes

*Analytical model approximates the rough surface impulse response with a Gaussian function; Semi-analytical model includes numerical integration of the impulse response and convolution with transmit signal and surface height PDF; Numerical model is a fully-numerical simulation of the backscattered SAR echo

nadir leads can be detected up to the antenna beam-limited footprint radius ~7.5 km off nadir [16]. Past studies have mitigated for these uncertainties by discarding a portion of atypical waveforms not falling into any single class e.g. [5, 17, 18]; however, mixed waveforms that are not discarded can still introduce biases into sea surface height retrievals [16].

At the near-nadir incidence angles of a radar altimeter, it is assumed the Ku-band wave is principally backscattered from the snow-ice interface [19]. The most common approach for identifying (or 'retracking') the principal scattering horizon of a sea ice echo is the empirical Threshold First-Maximum Retracking Algorithm (TFMRA), which records the retracking range at a predefined threshold of the first major power peak [5]. A threshold of 50% power, adopted from pulse-limited altimetry, has been used most often [5, 6, 18, 20], although a higher threshold of 60-70% has demonstrated the closest association with validation data [6]. Variable thresholds can be applied for retracking sea ice versus lead returns [6]. Using a physically-based retracking model, Kurtz et al. [17] estimated that, for a Gaussian sea ice surface height distribution, the correct threshold is closer to 85-95%. This range of thresholds corresponds to >0.5 m variation in elevation over the roughest sea ice. The true retracking threshold varies in response to several factors that affect the mean scattering elevation of the surface. (i) Processing methodology of the pulse-limited or SAR system. (ii) The fractional mix and location of scattering elements within the sensing footprint, i.e. snow, ice and water [21]. (iii) Primary footprint-scale (1-100s meter) surface roughness [17]. (iv) Secondary small-scale (0.001-1 meter) surface roughness [22, 23]. (v) Snow properties, including depth, grain size [24, 25] and basal and volume salinity [26].

Two generalized physical models have been developed to simulate backscattered Cryosat-2 echoes from sea ice, the CS2WfF model [17] and SAMOSA+ model [23] (Table I). By adapting SAR altimetry theory for open ocean [27, 28], the received radar echo in both models can be expressed as the double convolution of the compressed transmit pulse, the surface height probability density function (PDF) and the 'rough surface' impulse response. An additional convolution on the snow backscattering coefficient has been tested [17, 29]. (Note that several other semi-analytical models have been developed for the backscattered SAR altimeter echo from open ocean, e.g. [28, 30]). These models treat the target as a uniform, isotropic and homogenous, purely surface scattering medium and make the classical assumption that footprint-scale surface roughness can be represented by a Gaussian PDF. Both the homogenous and Gaussian simplifications are required to reduce the problem to a tractable level and obtain a generalized solution; however, they each have limited validity for sea ice surfaces.

Rivas et al. [31] found that only 1% of their sea ice roughness observations (over the thinnest most-level ice) could be accurately represented by a Gaussian PDF. Numerous studies have demonstrated that sea ice surface roughness and thickness distributions are better represented by a lognormal PDF [32, 33, 34, 35, 36, 37]. However, it is not only the sea ice height PDF that is assumed to be Gaussian. Both above models use a formal definition for the impulse response that is derived by assuming a Gaussian surface height distribution (Table I). The reduction in backscatter from a rough ocean surface as a function of radar incidence angle (the backscattering efficiency) can be well explained by a scattering model assuming Gaussian height statistics [38]. CS2WfF adapts the Hagfors [39] scattering model (which assumes an undulating Gaussian height PDF but exponentially autocorrelated surface) to calculate the sea ice backscattering efficiency as a function of secondary-scale roughness. Likewise, SAMOSA+ uses the same definition of the impulse response as the SAMOSA-2 ocean echo model [27] but introduces a term to parameterize the 'scattering amplitude decay' in terms of the secondary-scale surface roughness (in this case the mean-square slope) [23]. Neither of these models can correctly simulate the impulse response from a sea ice surface with lognormal, fractal or other potentially more realistic height statistics.

Our long-term goal is to investigate the sensitivity of SAR altimeter echoes from sea ice to surface roughness (at multiple scales), mixed surface types, and snow & ice thermophysical properties. As a tool designed to realize these objectives, we present a new facet-based numerical model for simulating delay-Doppler SAR altimeter echoes from snow-covered sea ice with prescribed statistical or real surface height topography. The effect of nadir-located or off-nadir leads can also be included in the model to enable examination of the contributions of different scattering mechanisms within the antenna footprint to the total echo. In (II) we introduce the numerical model, including the method used to generate triangular facet models of statistical surface topographies, the facet-based delay-Doppler SAR altimeter echo simulator, and

the surface & volume backscattering properties of snow, sea ice and leads. In (III) we demonstrate the model sensitivity, first to parameters of the Cryosat-2 SIRAL instrument (pitch, roll, altitude) and second to properties of the target (snow & ice geophysical properties, surface roughness characteristics, mixed surface types). In (IV) we apply the model to a set of Operation IceBridge airborne laser scanning data of sea ice topography from the Central Arctic Ocean and compare simulated echoes to real echoes from a coincident Cryosat-2 overpass. Finally, in (V) we compare the facet-based model to SAMOSA+ and discuss potential applications for the new simulator, before concluding in (VI).

II. NUMERICAL ECHO MODEL

A. Rough Surface Simulation

Three different types of statistical rough surface are generated, using spectral analysis, to represent the primary footprint-scale (1-100s meters) sea ice surface topography. The predetermined parameters used to characterize all these surfaces are the root-mean square roughness height σ_{surf} and autocorrelation length l_{surf}. The power spectrum of sea ice surface roughness can be well described by a Lorentzian model (i.e. height features are exponentially correlated [31]), so we first generate surfaces with Gaussian height distributions and exponential autocorrelation functions. Gaussian height statistics are randomly drawn from the following zero-mean PDF

$$f(z) = \frac{1}{\sqrt{2\pi{\sigma_{surf}}^2}} e^{-\frac{z^2}{2{\sigma_{surf}}^2}} \quad (1)$$

(which has been adopted to represent the sea ice topography in both CS2WfF and SAMOSA+), to generate an initially uncorrelated rough surface. The correlated surface is derived by multiplying the Fourier transform of $f(z)$ with the root of the Fourier transform of the autocorrelation function $\omega(\xi) = e^{-|\xi|/l_{surf}}$, following the method of [40]. Surfaces with a lognormal height distribution and exponential autocorrelation function are generated in a similar manner, following the approach of [41]. In this case, height statistics are drawn from the following PDF

$$f(z) = \frac{1}{z\sigma_{log}\sqrt{2\pi}} e^{-\frac{(\ln z - \mu_{log})^2}{2{\sigma_{log}}^2}} \quad (2)$$

and σ_{log} and μ_{log} can be related to σ_{surf} by

$$\sigma_{surf} = \sqrt{\left(e^{{\sigma_{log}}^2} - 1\right) e^{\left(2\mu_{log} + {\sigma_{log}}^2\right)}}$$
$$e^{\left(\mu_{log} + \frac{{\sigma_{log}}^2}{2}\right)} = 0. \quad (3)$$

Finally, random fractal surfaces are generated from a roughness spectrum with a Gaussian height distribution, characterized by rms height σ_{surf} and a high spatial-wavelength cutoff at $\frac{2\pi}{l_{surf}\Delta x}$, where Δx is the sampling interval of the surface [42]. The slope of the spectrum is controlled by a third surface parameter, the Hurst exponent H_{surf}, which is related to the fractal dimension of the surface by $D = 3 - H_{surf}$. The two scale parameters σ_{surf} and l_{surf} can be selected independently for each surface and do not depend on the choice of height PDF. Past observations have demonstrated that sea ice roughness parameters vary in the range $0.05 < \sigma_{surf} < 0.50$ m and $1 < l_{surf} < 10$ m, between smooth level first-year ice and deformed multi-year ice [31, 33, 34]. After a surface is generated it is converted into a triangular irregular network (TIN) based on the *MATLAB* Delaunay triangulation structure. This structure contains a set of vectors defining the vertices or nodes of the original surface and the continuous tetrahedral mesh which links them. Our facet-based model computes the SAR altimeter's power waveform from the integral of power backscattered from each triangular facet of the tetrahedral mesh.

TABLE II
SYSTEM PARAMETERS USED IN THE NUMERICAL ECHO MODEL

Symbol	Parameter	Reference Value
c	Speed of light	299792458 m s-1
R_e	Radius of Earth	6371000 m
λ_0	Carrier wavelength	0.0221 m
k_0	Carrier wavenumber	284.307 m-1
B_w	Received bandwidth	320000000 Hz
h	Satellite altitude	720000 m
v	Satellite velocity	7500 m s-1
f_p	Pulse repetition frequency	18182 Hz
P_T	Transmit peak power	2.2 x 10-5 W
G_0	One-way antenna gain	42 dB
D_0	Synthetic beam gain	36.12 dB
γ_1	Along-track antenna parameter	0.0116 rads
γ_2	Across-track antenna parameter	0.0129 rads
N_b	Number of synthetic beams	64

B. Delay-Doppler SAR Altimeter Echo Model

We base our SAR altimeter echo model on the sensing and processing infrastructure of the Cryosat-2 SIRAL instrument. SIRAL uses aperture synthesis to generate a set of N_b Doppler beams equally spaced in angle over the antenna's along-track beam-width, for every burst of radar pulses. The angular interval between successive Doppler beams is [28]

$$\xi_k = \frac{\lambda_0 f_p}{2N_b v} \quad (4)$$

(see Table II for parameter definitions). Each synthetic beam illuminates a beam-limited footprint along the satellite track of width

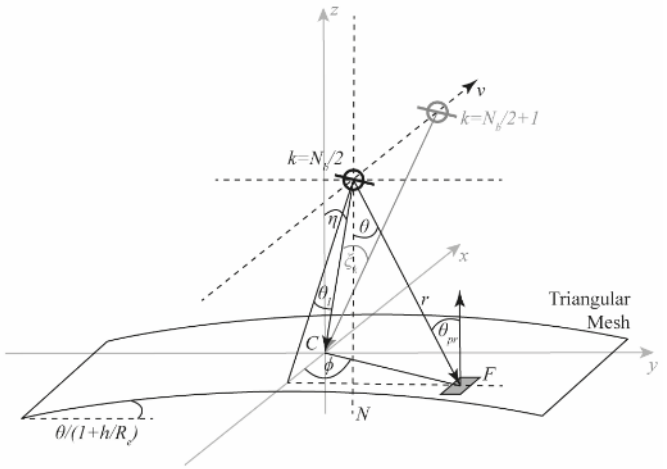

Fig. 1. Three-dimensional geometry of the facet-based SAR altimeter echo model. The triangular mesh is always located such that the antenna boresight is directed towards the surface centre *C* at $x = 0$ and $y = 0$. The satellite velocity vector v is aligned to the x-axis but rolled by angle η so that the radar is mis-pointing along the y-axis and the nadir location *N* does not align with *C*. Synthetic beams are formed at a series of look angles with interval ξ_k, parallel to the x-axis, between the synthetic beam boresight direction and *C*. Here the angles are illustrated from the central beam $N_b/2$ and subsequent beam $N_b/2 + 1$, having been 'steered' to the identical sub-satellite location *C*. Surface facet *F* is located at azimuth angle ϕ in the xy-plane and incidence angle θ from *N*, with respect to the satellite origin $\ominus$ at beam $N_b/2$. The satellite 'look angle' to *F* is characterized only in the xz-plane and is given by θ_l. The polar response angle θ_{pr} of *F* is the difference between the antenna-facet vector $\ominus F$ and facet normal-vector.

$$\Delta x_{dopp} = h\xi_k \tag{5}$$

while remaining pulse-limited across-track to

$$\Delta x_{pl} = 2\sqrt{\frac{c}{B_w}\frac{hR_e}{h+R_e}}. \tag{6}$$

Equations (5) and (6) define the area of the triangular mesh generated in Section II-A. Doppler cells illuminated at different angles, but from consecutive bursts, can subsequently be 'steered' to the same location on the surface, providing N_l independent looks at the surface within a small range of angles limited to $N_b\xi_k$ [11]. The actual number of looks in a multi-looked SAR waveform can be as high as 240 [28]. The set of N_l co-located radar echoes can be 'stacked' by performing a slant-range correction to compensate for the increased two-way transit time of echoes from off-nadir Doppler beams. Slant-range time correction τ_c for the k^{th} Doppler beam is

$$\tau_c(k) = \frac{2}{c}\sqrt{\left(\frac{k\xi_k}{h}\right)^2\left(1+\frac{h}{R_e}\right)+h^2} \tag{7}$$

which accounts for curvature of the Earth's surface. The final 'multi-looked' Cryosat-2 SAR-mode waveform is an incoherent sum of all the independent echoes (or looks) from the stack, which reduces speckle noise and improves the measurement precision [11]. Here, we do not introduce speckle to the modelled echo and therefore do not have to account for N_l. The multi-looked waveform can be characterized exactly from $N_b = 64$.

The multi-looked echo waveform model is based on the following power integral, which calculates a stack of N_b received echoes from a prescribed rough surface using the radar equation [43, 44, 45]

$$P_r(\tau) = \sum_{k=-(N_b-1)/2}^{(N_b-1)/2} \frac{{\lambda_0}^2 P_T}{(4\pi)^3}\left(\frac{1}{2}ch\right) \int_A \frac{p_T(\tau,k)}{r^4} G^2(\theta,\phi) d(\xi_k)\sigma^0(\tau,\theta_{pr})\, dA \tag{8}$$

where A is the area of a surface facet, $p_T(\tau,k)$ describes the transmitted power envelope as a function of time τ and synthetic beam k, r is the range, $G(\theta,\phi)$ is the antenna gain pattern as a function of incidence θ and azimuth ϕ angles, $d(\xi_k)$ describes the gain pattern of synthetic beam k as a function of look-angle ξ_k during along-track SAR processing, and $\sigma^0(\tau,\theta_{pr})$ describes the total surface plus volume backscattering coefficient as a function of time and facet polar response angle θ_{pr}. The basic geometry of the echo model is illustrated in Figure 1. While the location of the triangular mesh is fixed, so the antenna boresight is always directed towards the surface centre, the antenna origin depends on satellite altitude, pitch ζ and roll η mis-pointing angles, and Doppler beam angle

$$\begin{aligned} x_0 &= hk\xi_k + h\zeta \\ y_0 &= h\eta \end{aligned} \tag{9}$$

The range, incidence angle and azimuth angle from the antenna origin to surface facet $[x_i, y_i, z_i]$ are therefore

$$\begin{aligned} r &= \sqrt{(z_i-h)^2 + [(x_i-x_0)^2+(y_i-y_0)^2]\left(1+\frac{h}{R_e}\right)} \\ \theta &= \frac{\pi}{2} + \tan^{-1}\left[\frac{\sqrt{(x_i-x_0)^2+(y_i-y_0)^2}}{(z_i-h)}\right] \\ \phi &= \tan^{-1}\left(\frac{x_i-x_0}{y_i-y_0}\right) \end{aligned} \tag{10}$$

The polar response angle θ_{pr} is simply the angle between the antenna-facet vector and facet-normal vector [43]. As the antenna boresight is directed towards the surface centre, the look angle between the radar and facet with respect to the xz-plane is given by

$$\theta_l = \tan^{-1}\left(-\frac{x_i - hk\xi_k}{z_i - h}\right) \tag{11}$$

The transmitted compressed pulse of the SIRAL radar can be described by a sinc function

$$p_T(\tau) = sinc^2(\pi B_w \tau) \tag{12}$$

where τ is the time referenced to the mean scattering surface of the echo, given by

$$\tau = t + \tau_c(k) - \frac{2r}{c} \quad (13)$$

where t defines the sampling of bins n (1 to 256 for Cryosat-2 in SAR mode) in the altimeter ranging window $t = \frac{1}{2B_w}(n - t_0)$, and t_0 is the bin number at the mean sea ice elevation. The mean ice elevation is necessary for accurately calculating the sea ice freeboard, rather than any other parameter of the ice surface height distribution. The synthetic beam gain function is adapted from [11, 44] as

$$D_0 d(\xi_k) = \left| \frac{\sin\left(N_b \left[k_0 \frac{v}{f_p} \sin(\theta_l + k\xi_k)\right]\right)}{N_b \sin\left(k_0 \frac{v}{f_p} \sin(\theta_l + k\xi_k)\right)} \right|^2 \quad (14)$$

where D_0 is the gain of a single beam. In the Cryosat-2 processing chain, a Hamming window is conventionally applied to (14) in the along-track direction, during synthetic aperture processing, to reduce scattering ambiguities introduced by side-lobes of the synthetic beam

$$H = 0.54 - 0.46 \cos\theta_l \quad (15)$$

Finally, the elliptical pattern for the SIRAL antenna's gain is established as [11]

$$G(\theta, \phi) = G_0 exp\left[-\theta^2 \left(\frac{\cos^2\theta}{{\gamma_1}^2} + \frac{sin^2\,\phi}{{\gamma_2}^2}\right)\right] \quad (16)$$

Giles et al. [43] demonstrated that the integral in (8) could be approximated as a sum provided the surface facets over which the power is integrated are small enough. As the transmitted pulse intersects the surface, the pulse annulus decreases in width. An error is introduced if the facet spacing is so coarse that the annulus cannot be effectively defined, with the error increasing (by power 2) over echo time. By testing the model over a very rough surface (σ_{surf} = 0.5 m), we found that the minimum facet spacing required before significant error is introduced to the echo trailing edge is ~25 m. This is well above the upper spacing limit necessary for characterizing the surface backscattering coefficient, as described in Section II. C, and thus does not impact our simulations.

C. Surface and Volume Backscatter Modelling

Estimating the backscattering coefficient σ^0 of a sea ice surface with nonuniform topography, potentially also containing mixed surface types including leads at the footprint scale, is a major source of uncertainty in the echo model. The ice surface backscattered power has been estimated in previous studies using simple exponential or power-law functions. For instance, Giles et al. [43] adopted the following expression

$$\sigma^0(\theta_{pr}) = exp\left(-\frac{\theta_{pr}}{\phi_{pr}}\right)^2 \quad (17)$$

TABLE III
REFERENCE VALUES AND EXPECTED RANGES OF VALUES FOR PARAMETERS USED IN SURFACE AND VOLUME BACKSCATTER MODELLING OF SNOW, SEA ICE AND SEAWATER.

	Parameter	Expected Range	Reference Value	
$\boldsymbol{\sigma_s}$	Air-snow rms height	0.5 to 2.0 mm	1 mm	[22, 67]
$\boldsymbol{l_s}$	Air-snow correlation length	10 to 100 mm	40 mm	[22, 67]
$\boldsymbol{T_s}$	Bulk snow temperature	-30 to -5 °C	-20 °C	[68]
$\boldsymbol{\rho_s}$	Bulk snow density	50 to 450 kg m^{-3}	350 kg m^{-3}	[69]
$\boldsymbol{\chi_s}$	Snow grain size	0.05 to 4.00 mm	1 mm	[14, 69]
$\boldsymbol{h_s}$	Snow depth	0 to 50 cm	25 cm	[66]
$\boldsymbol{\sigma_{si}}$	Snow-ice rms height	1 to 4 mm	2 mm	[22, 67]
$\boldsymbol{l_{si}}$	Snow-ice correlation length	5 to 40 mm	20 mm	[22, 67]
$\boldsymbol{T_{si}}$	Bulk sea ice temperature	-20 to -2 °C	-15 °C	[68]
$\boldsymbol{S_{si}}$	Bulk sea ice salinity	2 to 12 ‰	6 ‰	[68]
$\boldsymbol{\sigma_{sw}}$	Seawater-air rms height	0 to 0.01 mm	0.001 mm	[67]
$\boldsymbol{T_{sw}}$	Seawater temperature	-2 to 0 °C	0 °C	[68]
$\boldsymbol{S_{sw}}$	Seawater salinity	28 to 35 ‰	34 ‰	[68]
$\boldsymbol{\beta_c}$	Effective angular width of coherent scattering component	0 to ξ_k	ξ_k	[19]

where ϕ_{pr} is the backscattering efficiency, which defines the rate that backscattered power drops off as the facet-normal diverges from the antenna boresight direction. This is a similar approach to Kurtz et al. [17] who quantified σ^0 as a function of secondary-scale sea ice surface roughness

$$\sigma^0(\theta_{pr}) = \frac{R_0 \alpha}{2}\left(1 + \alpha \sin^2\theta_{pr}\right)^{\frac{-3}{2}} \quad (18)$$

where R_0 is the Fresnel reflection coefficient at normal incidence, $\alpha = \left(\frac{l_{si}}{2k_0{\sigma_{si}}^2}\right)^2$, and σ_{si} and l_{si} are the small-scale sea ice rms height and autocorrelation length. Note that σ_{si} and l_{si} parameterize roughness in the same way as σ_{surf} and l_{surf}; however, the two parameter sets are completely independent. The latter applies only to the generation of large-scale ice surface topography, as described in Section II-A, whereas the former applies only to small-scale roughness in the IEM simulations described below. The functions in (17) and (18) are illustrated in Figure 2, with representative values of ϕ_{pr} and α for diffuse sea ice-type and specular lead-type surfaces.

Here we model the backscattering coefficient directly by simulating surface scattering properties of snow, sea ice and seawater, as well as volume scattering by snow, and by accounting for their individual contributions to the total backscattered power within the altimeter footprint. Several initial assumptions are necessary to simplify the problem. We assume zero volume backscatter from sea ice [46], with all the energy transmitted across the snow-ice interface absorbed by

the ice cover. We model scattering and absorption in the snow cover, if present, but here only consider dry snow (T_s < -5 °C) in a single layer, neglecting any dependence on salinity or liquid water in the snowpack. Additionally, we make the reasonable assumption that surface scattering of the Ku-band wave from air-snow and snow-ice interfaces is purely diffuse and estimate only incoherent backscatter [47]. In contrast, we assume the seawater surface in a lead is a purely specular reflector and estimate only the coherently reflected power.

1) Snow and Ice Surface Scattering

Surface backscattering coefficients from air-snow and snow-ice interfaces are modelled using the integral equation model (IEM) for polarization pp [48, 49]

$$\sigma_{pp}^0 = \frac{k_0^2}{4\pi} exp(-2k_z^2\sigma_m^2) \sum_{n=1}^{\infty} |I_{pp}^n|^2 \frac{W^{(n)}(-2k_x, 0)}{n!} \quad (19)$$

where $k_z = k_0 \cos\theta_{pr}$, $k_x = k_0 \sin\theta_{pr}$, pp = VV or HH, σ_m is the rms height for medium m (snow or ice), and $W^{(n)}$ is the Fourier transform of the n^{th} power of the surface autocorrelation function (ACF). The ACF of natural small-scale snow and sea ice surfaces can be well characterised by the exponential function $\omega(\xi) = e^{-|\xi|/l_m}$ [22]. The spectrum I_{pp}^n is defined as [48, 49]

$$I_{pp}^n = (2k_z\sigma_m)^n f_{pp} exp(-k_z^2\sigma_m^2) + (k_z\sigma_m)^n F_{pp} \quad (20)$$

where the coefficients

$$f_{VV} = \frac{2R_V}{cos\theta_{pr}};\ f_{HH} = \frac{-2R_H}{cos\theta_{pr}} \quad (21)$$

$$F_{VV} = \left(\frac{\sin^2\theta_{pr}}{cos\theta_{pr}} - \frac{\sqrt{\mu_m\varepsilon_m - \sin^2\theta_{pr}}}{\varepsilon_m}\right)(1+R_V)^2 - 2\sin^2\theta_{pr}\left(\frac{1}{cos\theta_{pr}} - \frac{1}{\sqrt{\mu_m\varepsilon_m - \sin^2\theta_{pr}}}\right)(1+R_V)(1-R_V) + \left(\frac{\sin^2\theta_{pr}}{cos\theta_{pr}} - \frac{\varepsilon_m(1+\sin^2\theta_{pr})}{\sqrt{\mu_m\varepsilon_m - \sin^2\theta_{pr}}}\right)(1-R_V)^2 \quad (22)$$

$$F_{HH} = -\left(\frac{\sin^2\theta_{pr}}{cos\theta_{pr}} - \frac{\sqrt{\mu_m\varepsilon_m - \sin^2\theta_{pr}}}{\mu_m}\right)(1+R_H)^2 + 2\sin^2\theta_{pr}\left(\frac{1}{cos\theta_{pr}} - \frac{1}{\sqrt{\mu_m\varepsilon_m - \sin^2\theta_{pr}}}\right)(1+R_H)(1-R_H) - \left(\frac{\sin^2\theta_{pr}}{cos\theta_{pr}} - \frac{\mu_m(1+\sin^2\theta_{pr})}{\sqrt{\mu_m\varepsilon_m - \sin^2\theta_{pr}}}\right)(1-R_H)^2 \quad (23)$$

R_V and R_H are the Fresnel reflection coefficients for H and V polarisations, μ_m is the relative permeability of medium m, and $\varepsilon_m = \varepsilon_m' + i\varepsilon_m''$, are real ε' and imaginary ε'' parts of the complex dielectric permittivity of the medium. The SIRAL antennas are linearly polarized with an orientation parallel to the interferometer baseline [11], which means that effective polarization varies with ϕ. Because of this we estimate final surface σ^0 simply from the mean of σ_{VV}^0 and σ_{HH}^0. In any case σ_{VV}^0 and σ_{HH}^0 are almost identical at low incidence angles. The presented derivation of the IEM is valid for $k_0\sigma_m$ < 2 and $\sqrt{3}\frac{\sigma_m}{l_m}$ < 0.3 [48], which for Ku-band places an upper limit on σ_m of ~7 mm and a lower limit on l_m of ~10 mm, suitable for the realistic range of interface roughness values in Table III. Owing to the multi-scale nature of sea ice roughness, field

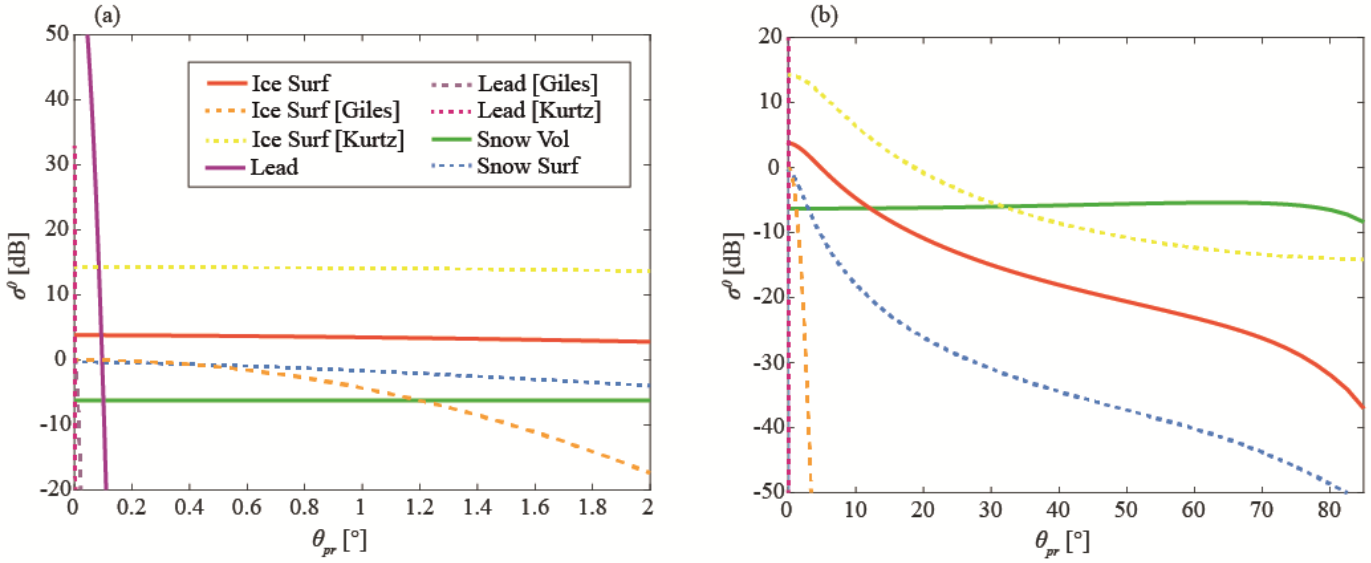

Fig. 2. Backscattering coefficients σ^0 of snow, sea ice and leads, simulated by various methods. Panel (a) is a subset of panel (b) covering only the 0-2° incidence angle range. Snow volume (vol) & surface (surf) scattering, sea ice surface scattering and lead scattering coefficients are modelled directly from Eqs. (19)-(32), using the parameter set in Table III. Estimates for sea ice and lead surface backscattering coefficients are also obtained following the techniques of [17, 43]. ϕ_{pr} in (17) is taken as 1° and 0.01° for diffuse and specular surfaces, respectively. σ_{si} and l_{si} in (18) are taken as 2 and 20 mm for the diffuse surface and 0.01 and 1000 mm for the specular surface.

measurements of these small-scale roughness parameters tend to depend on the length-scale at which they are characterized. For instance, Landy et al. [22] demonstrated that measured small-scale roughness parameters remain within the IEM validity criteria only up to a length-scale of a few meters. It is not computationally practical to run our numerical echo model on a triangular mesh of 1-m facets, so we generally use 5-m facets for the simulations as a compromise between speed and accuracy.

The dielectric constants of snow, sea ice and seawater are frequency dependent, and are derived here for the Ku-band. The relative dielectric constant of pure ice is estimated from the model introduced by Mätzler [50], depending weakly on temperature, but generally ε_i = 3.175 + 0.001i. The dry snow dielectric constant is obtained from an empirical expression in [50], derived from a two-phase Tinga-Voss-Blossey (TVB) mixing formula for spherical pure ice particles interspersed in air and with bulk density ρ_s. Snow dielectric constant depends strongly on density but, based on the reference values for T_s and ρ_s in Table III, ε_s = 1.640 + 0.000i. The sea ice is treated as a heterogenous mixture of liquid brine inclusions interspersed within a pure ice host medium. The dielectric constant of brine is derived from the formulations of Stogryn [51], which require an estimate for the brine salinity. This is obtained from the well-known brine salinity S_b and volume V_b functions of bulk sea ice temperature T_{si} and salinity S_{si} developed by Cox and Weeks [52]. With the reference values for T_{si} and S_{si}, brine permittivity ε_{br} = 12.3 + 19.0i. A sea ice dielectric constant is estimated from a TVB mixing formula for spherical brine inclusions with volume fraction V_b/V_{si}, in a background of pure ice, and is ε_{si} = 3.35 + 0.06i. A seawater dielectric constant is derived through the same method as brine [51] and is ε_{sw} = 29.5 + 36.7i. Realistic variations in sea ice and seawater dielectric constants do not significantly affect the modelled echo; however, snow dielectric properties, depending on density and grain size, are significant and therefore analyzed directly in Section IV-B.

2) Lead Surface Scattering

We expect the radar wave to be reflected coherently from a smooth lead within the ice pack, providing high backscattered power close to the nadir location but reducing quickly as θ rises. In the general case, the total polarization-independent monostatic scattering coefficient $\sigma^0(\theta) = \sigma^0_{coh}(\theta) + \sigma^0_{inc}(\theta)$, consisting of coherent and incoherent components, respectively. For a given lead surface roughness, the fraction of the backscattered power reflected coherently (rather than scattered incoherently) is [19]

$$\omega_{coh} = exp(-2k_0\sigma_{sw}cos\theta)^2 \tag{24}$$

For a lead surface with very low roughness (i.e. in the absence of significant wind-wave roughening) ω_{coh} is above 0.98, so we assume the lead only contributes coherently reflected power. Using (24), the coherent backscattering coefficient can be defined in terms of the surface roughness and the Fresnel reflection coefficient as [19]

$$\sigma^0_{coh} = \pi {k_0}^2 |2R\cos\theta|^2 \exp(-2k_0\sigma cos\theta)^2 \delta(2k_0 sin\theta) \tag{25}$$

where δ is the Dirac delta function. The delta function accounts for the fact that the coherent contribution exists only at angles θ in the immediate vicinity of normal incidence. By approximating $\cos\theta \cong 1$ and $\sin\theta \cong \theta$, and taking $\delta(2k_0 sin\theta)$ to be Gaussian in shape, the coherent backscattering coefficient for a smooth seawater surface can then be written in the form [53]

$$\sigma^0_{sw} = \left(\frac{R}{\beta_c}\right)^2 \exp(-4k_0^2\sigma_{sw}^2) exp\left(-\frac{\theta^2}{\beta_c^2}\right) \tag{26}$$

where β_c is the effective width of the angular extent of the coherent backscatter component σ^0_{sw}. Equation (26) is valid only at small angles, for close to specular surfaces, and the magnitude of β_c is generally smaller than 1°. For SIRAL, β_c is limited to a maximum angle of ξ_k but, in the absence of sufficient calibration data over leads, we take $\beta_c = \xi_k$ as a first approximation.

3) Snow Volume Scattering

Volume scattering and absorption within the snowpack are estimated from Mie scattering theory, for ice particles of radius χ_s with density ρ_s. At realistic snow grain sizes (χ_s > 0.5 mm) scattering dominates absorption in dry snow at frequencies around 15 GHz and above [46] and grain sizes are too large to use the Rayleigh approximation [19]. The snow volume scattering coefficient does not depend on polarization. We assume a single snow grain size and no additional scattering contribution from brine present in the snow volume [26]. The single scattering, extinction and absorption efficiencies of a spherical ice particle can be calculated from [19]

$$\begin{aligned} \zeta_s &= \frac{2}{\psi^2}\sum_{l=1}^{\infty}(2l+1)(|a_l|^2 - |b_l|^2) \\ \zeta_e &= \frac{2}{\psi^2}\sum_{l=1}^{\infty}(2l+1)\Re\{a_l + b_l\} \\ \zeta_a &= \zeta_e - \zeta_s \end{aligned} \tag{27}$$

where $\psi = \frac{2\pi\chi_s}{\lambda_0}$, $n = \sqrt{\frac{\varepsilon_i}{\varepsilon_a}}$, and the relative permittivity of air ε_a = 1. The coefficients in (27) are calculated from the recursive procedure

$$\begin{aligned} a_l &= \frac{\left(\frac{A_l}{n} + \frac{l}{\psi}\right)\Re\{W_l\} - \Re\{W_{l-1}\}}{\left(\frac{A_l}{n} + \frac{l}{\psi}\right)W_l - W_{l-1}} \\ b_l &= \frac{\left(nA_l + \frac{l}{\psi}\right)\Re\{W_l\} - \Re\{W_{l-1}\}}{\left(nA_l + \frac{l}{\psi}\right)W_l - W_{l-1}} \end{aligned} \tag{28}$$

where $W_l = \left(\frac{2l-1}{\psi}\right)W_{l-1} - W_{l-2}$, and $A_l = -\frac{l}{n\psi} + \left(\frac{l}{n\psi} - A_{l-1}\right)^{-1}$. Here the notation $\Re\{W_l\}$ describes the real part of the

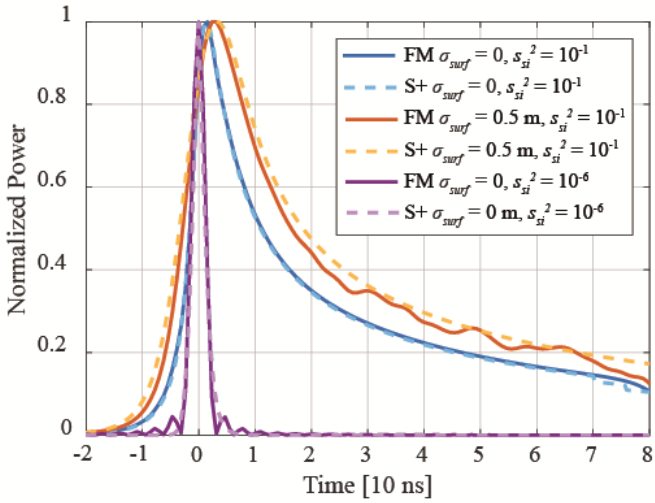

Fig. 3. SAR echoes from sea ice simulated with the facet-based numerical model presented here ('FM', solid lines) and the semi-analytical generalized isotropic model SAMOSA+ ('S+', dashed lines).

function W_l, where $W_0 = sin\psi + jcos\psi$ and $W_{-1} = cos\psi - jsin\psi$. The scattering, extinction and absorption coefficients κ_v of snow can then determined from

$$\kappa_v = \pi {\chi_s}^2 N_v \zeta_v \tag{29}$$

where $N_v = \frac{\rho_s}{\rho_i}\left(\frac{4}{3}\pi\chi_s^3\right)^{-1}$ is the number density of ice spheres. For the reference snowpack properties (Table III) scattering dominates absorption: scattering coefficient κ_s = 7.8 dB m^{-1}, absorption coefficient κ_a = 0.3 dB m^{-1}, so that extinction coefficient κ_e = 8.1 dB m^{-1}. The snow volume backscattering coefficient is estimated from the extinction coefficient and snow depth h_s as [47]

$$\sigma^0_{s\ vol} = T(\theta_T)^2\left[1 - exp\left(\frac{-2\kappa_e h_s}{cos\theta_T}\right)\right] \tag{30}$$

where T is the Fresnel transmission coefficient at the air-snow interface, and $\theta_T = \sin^{-1}\left(\sin\theta_{pr}\sqrt{\varepsilon_a/\varepsilon_s}\right)$ is the angle of transmission into the snowpack.

4) Total Backscattering Coefficient

The total backscattering coefficient for a facet as a function of antenna-facet polar incidence angle θ_{pr} and echo time τ can be calculated from (19), (26) and (30) as [17, 44, 29]

$$\sigma^0(\tau,\theta_{pr}) = \begin{cases} 0, \tau < -\dfrac{2h_s}{c_s} \\ \sigma^0_{s\ surf}(\theta_{pr}) + \sigma^0_{s\ vol}(\tau,\theta_{pr})\kappa_e \\ exp\left[-c_s\kappa_e\left(\tau + \dfrac{2h_s}{c_s}\right)\right], -\dfrac{2h_s}{c_s} \geq \tau > 0 \\ \sigma^0_{si}(\theta_{pr})T(\theta_T)^2 exp\left(-\dfrac{\kappa_e h_s}{2}\right), \tau \geq 0 \\ \sigma^0_{sw}(\theta_{pr}), h_i = 0 \end{cases} \tag{31}$$

where the reduced speed of light within the snowpack is obtained from [13]

$$c_s = c(1 + 51\cdot 10^{-5}\sigma_s)^{\left(-\frac{3}{2}\right)}. \tag{32}$$

Total σ^0 can be integrated over the altimeter footprint within (8) to simulate the aggregate backscattered power of a multi-looked echo. However, each of the component backscattering coefficients (snow surface, snow volume, ice surface, lead surface) can also be integrated individually over the altimeter footprint to produce a set of multi-looked component echoes, as we demonstrate in Section IV. It is not computationally efficient to run forward models for the component backscattering coefficients at the θ_{pr} of each elevation model facet. Instead we fit cubic splines to smoothly-varying functions of σ^0, for each component, simulated for the full 0 to π/2 range of possible θ_{pr} values, but with interval spacing logarithmically weighted towards angles close to nadir. Spline interpolants can then be called for all facet θ_{pr} simultaneously.

III. COMPARISON WITH THE GENERALIZED MODEL SAMOSA+

The semi-analytical SAR waveform model SAMOSA+ is an adapted version of the generalized SAMOSA2 model for altimeter echoes from the ocean [27], developed for coastal altimetry but also applied for retracking waveforms from inland water and sea ice [23]. For quasi-specular surfaces the significant wave height (i.e. large-scale roughness) can be set to zero, with the mean-square slope of the surface (s_{si}^2) controlling how rapidly backscattering decays with incidence angle [23]. Here we evaluate how the facet-based SAR echo model for sea ice compares to waveforms simulated from SAMOSA+. The SAMOSA2 model approximates the point target impulse response (PTR) with a Gaussian curve and uses a Gaussian height PDF, so we compare SAMOSA+ echoes with varied s_{si}^2 to echoes simulated from the facet-based model with a Gaussian height distribution and varied σ_{si}. To relate s_{si}^2 to small-scale roughness σ_{si} and l_{si}, we use the following formula for the root mean-square slope of a truncated, exponentially-correlated surface [54]

$$s_{si} = \sqrt{\frac{2}{\pi}\frac{\sigma_{si}}{l_{si}}\sqrt{5k_0 l_{si} - \tan^{-1}(5k_0 l_{si})}}. \tag{33}$$

Figure 3 compares echoes simulated for a range of σ_{surf} from the facet-based model and SAMOSA+. We use a value of 0.42 for the SAMOSA+ coefficient α_p which approximates the dimensionless width of the PTR [23]. The facet-model and SAMOSA+ are almost identical for the flat surface response (σ_{surf} = 0), when small-scale roughness parameters are as in Table III. For a Gaussian PDF with σ_{surf} = 0.5 m, the echo from SAMOSA+ is slightly wider than the facet-model, with higher power modelled on the trailing edge. Some of this discrepancy may be explained by our use of constant α_p (whereas previous studies have treated this as an *a priori* unknown parameter [23]), or by the fact we parameterize surface autocorrelation l_{surf} directly. The specular echo from a lead is well

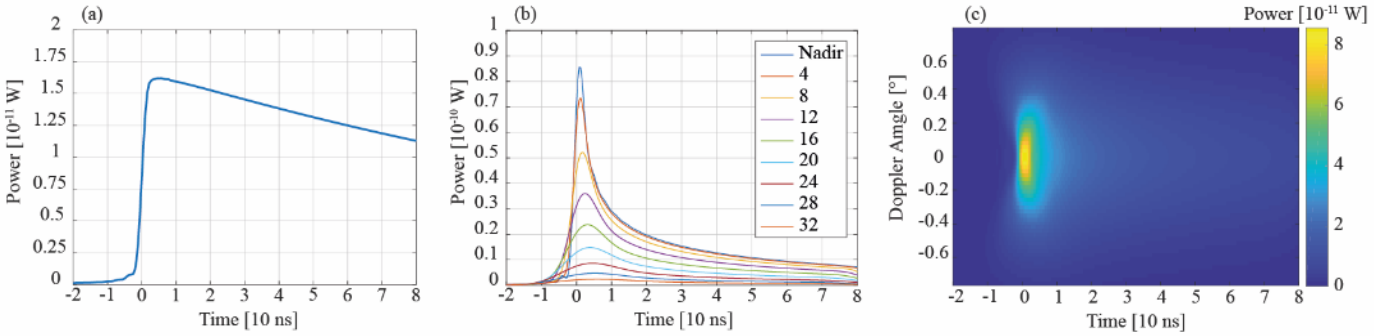

Fig. 4. Flat surface impulse response of sea ice simulated by the facet-based numerical echo model. Panel (a) is a single-look pulse-limited echo simulated from nadir. Panel (b) are SAR echoes simulated from various Doppler beams after slant-range time correction (7). Panel (c) is the full delay-Doppler map (DDM) simulated for N_b = 64, up to a maximum look angle of $\frac{N_b}{2}\xi_k$ = ±0.76°, as calculated from (4). All echoes are over-sampled in time by a factor of four for easier visualization.

characterized by a mean-square surface slope of 10^{-6}, when we set the effective width of the coherent reflection $\beta_c = \xi_k$.

IV. MODEL SENSITIVITY

By directly modelling the backscattering properties of snow, sea ice and seawater, and accounting for heterogeneity within the altimeter footprint, we can examine the sensitivity of the delay-Doppler SAR altimeter echo to fundamental target geophysical properties, as well as radar antenna parameters. We do not expect most of the geophysical parameters in Table III to significantly affect the echo shape, so in this section we generally illustrate only the most important parameters.

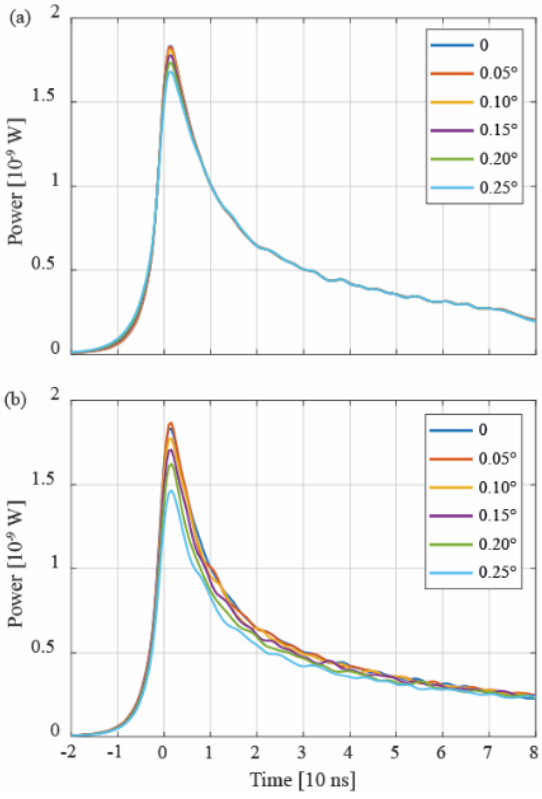

Fig. 5. Effect of mis-pointing in (a) pitch and (b) roll on SAR echoes from sea ice.

Reference parameter values from Tables II & III are used in all simulations unless otherwise stated.

A. Sensitivity to Antenna Parameters

The model applied to a perfectly level surface with h_s = 0 produces an echo analogous to the flat surface impulse response of sea ice. If the model is interrupted prior to SAR processing, a classic pulse-limited echo is simulated with the tracking point t_0 at half-power on the leading edge (Figure 4a). Contributions from a subset of different Doppler beams (Figure 4b) as part of the full delay-Doppler map (Figure 4c) highlights the variation in echo shape as a function of SAR look angle.

Our model provides an exact characterization of antenna boresight mis-pointing up to >0.25°; however, mean recorded pitch and roll of the Cryosat-2 antenna bench are less than 0.01° over Arctic regions [55]. The effects of mis-pointing in pitch ζ and roll η are illustrated in Figure 5, for a rough surface with lognormal PDF and exponential correlation function (σ_{surf} = 0.1 m, l_{surf} = 10 m), and indicate that realistic variations in satellite bench orientation do not significantly impact the backscattered waveform shape [27].

B. Sensitivity to Snow-Covered Sea Ice Physical Properties

1) Surface and Volume Backscattering Coefficients

The variation in backscattering coefficient σ^0 of a facet with incidence angle θ_{pr}, for different components of the ice cover (snow surface, snow volume, ice surface, lead surface), illustrates the potential heterogeneity in scattering mechanisms within the altimeter footprint (Figure 2). The three σ^0_{sw} scattering signatures are similar, with backscatter dropping off rapidly to negligible levels within θ_{pr} < 0.1°, reflecting the specular response of a lead. However, our direct estimation of σ^0_{sw} produces higher backscattering at nadir and falls off slightly less rapidly with θ_{pr} than the other parameterizations [17, 43]. Surface backscattering coefficients at air-snow and snow-ice interfaces have similar scattering signatures, although $\sigma^0_{s_{surf}}$ is significantly lower and drops off more rapidly than σ^0_{si} because the interface is smoother and dielectric contrast between snow and sea ice is larger [46, 48]. The shape of the power-law parameterization of [17] is a reasonable

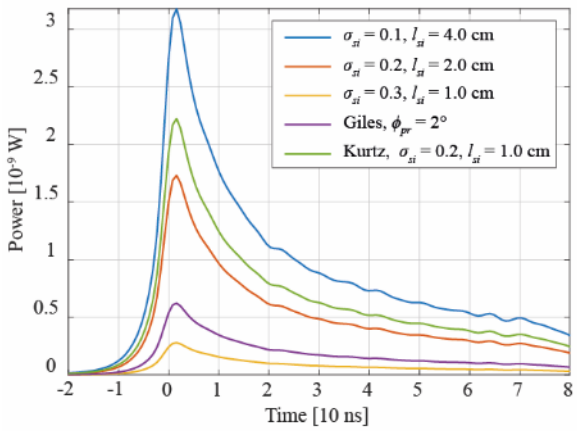

Fig. 6. Sensitivity of a SAR echo from sea ice to varied small-scale ice surface roughness parameterizations. For the Giles et al. [43] method, ϕ_{pr} in (17) was taken as 2° for a diffuse surface. For the Kurtz et al. [17] method, σ_{si} and l_{si} in (18) were taken as 2 and 10 mm to simulate a power response within the roughness bounds of the IEM simulations made here.

approximation for σ_{si}^0, although the absolute magnitude is lower than modelled σ_{si}^0 from IEM if the same roughness parameters are used. The exponential law of [43] overestimates the reduction in σ_{si}^0 as θ_{pr} rises above ~1°. Applying these three different parameterizations for σ_{si}^0 with varied small-scale roughness parameters to the numerical echo model, for a rough surface with lognormal PDF and exponential correlation function (σ_{surf} = 0.1 m, l_{surf} = 10 m, h_s = 0), produces the set of waveforms in Figure 6. The shape of the waveform is almost identical, but the waveform power (i.e. peak amplitude) and rate of trailing-edge decay are sensitive to variations in small-scale roughness. Finally, snow volume scattering is relatively low and remains almost constant over the relevant range of θ_{pr} for the altimeter echo model (Figure 2).

2) Model Sensitivity to Snow Properties

Snow cover at the sea ice surface shifts the tracking point of the echo forward by a time interval that depends on the physical properties of the snow: principally its depth. The backscattered echo is not sensitive to variations in snow surface roughness, within the realistic range of parameters tested here (Table III). However, at snow grain sizes χ_s > 1 mm volume scattering is significant, with the leading edge of the waveform shifting and becoming less concave (Figure 7a). Increasing snow density produces a similar response to larger grain size, with the leading edge beginning to shift when ρ_s > 150 kg m^{-3}, although not to the same degree (Figure 7b). Figure 7c illustrates that even 10 cm of accumulated snow has an instant effect on the waveform trailing edge. Backscattered power is reduced, but fluctuations also become enhanced because the reduced wave speed within the snowpack emphasizes small variations in sea ice topography between adjacent areas of the footprint. When volume scattering in the snowpack is strong, increasing snow depth shifts the tracking point to an earlier time, by up to $-\frac{2h_s}{c_s}$.

3) Model Sensitivity to Sea Ice Surface Roughness

Sea ice surfaces with large-scale topography simulated from a fractal roughness spectrum produce very similar echoes regardless of whether H_{surf} is 0 or 1. These surfaces also have a Gaussian PDF and therefore produce echoes close in shape to those simulated from an exponentially-correlated surface with a Gaussian PDF (Figure 8a). The clearest impact of representing the large-scale sea ice topography with a lognormal instead of conventional Gaussian PDF, is to reduce the amplitude of the tracking point on the waveform leading edge. For all waveforms, the tracking point corresponds to the mean height of the surface PDF and is used to obtain the range from satellite to surface. It therefore has a direct impact on the estimate of sea ice freeboard. The difference in tracking point threshold between lognormal and Gaussian surfaces becomes larger as surface roughness σ_{surf} increases. By an (unrealistic) roughness height of ~0.8 m (not shown), the tracking point for a lognormal surface is close to the 50% amplitude threshold adopted for pulse-limited waveform retracking [38] and regularly also for SAR waveform retracking from sea ice [5, 18].

Increasing σ_{surf} for a Gaussian surface has negligible impact on the amplitude threshold of the tracking point, but progressively widens echo leading and trailing edges (Figure 8b) [11, 17, 38]. This is because the mean scattering height of the ice surface is at approximately half the range in surface

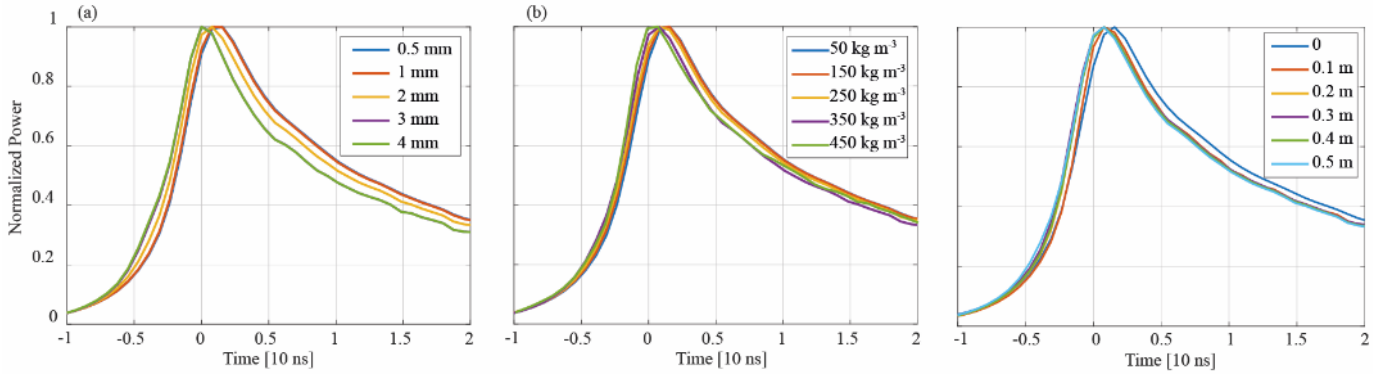

Fig. 7. Sensitivity of a SAR echo from sea ice to varied snow physical properties: (a) grain size, (b) density and (c) depth. All parameters are held at the values in Table III, with the exceptions that h_s = 0.5 m in (a) and (b), and χ_s = 2 mm in (b) and (c), to emphasize the results. The same large-scale sea ice surface topography is used as in Figure 6.

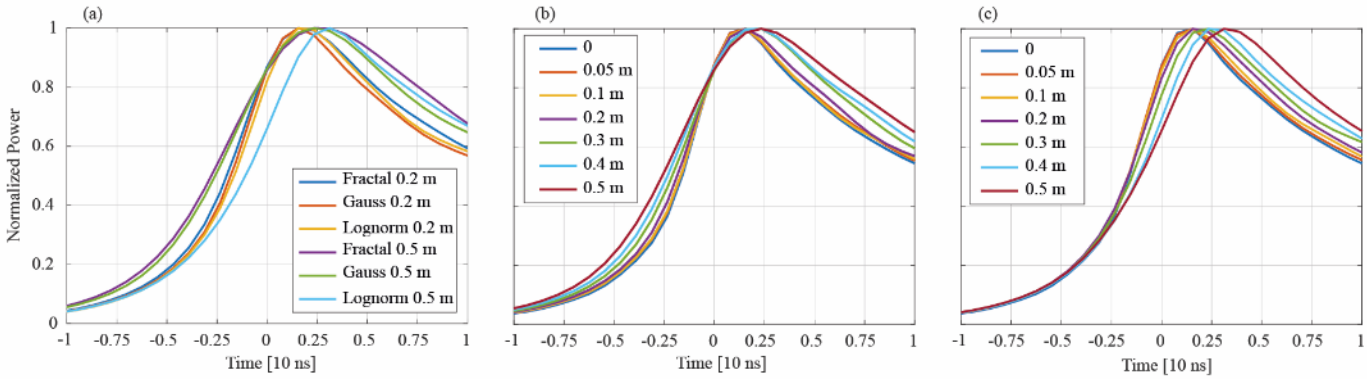

Fig. 8. Sensitivity of a SAR echo to large-scale sea ice surface roughness: (a) for Gaussian, lognormal and fractal surfaces simulated with the same roughness parameters; and surfaces with (b) lognormal and (c) Gaussian height distributions, constant correlation lengths l_{surf} = 5 m, but varied roughness heights σ_{surf}. Each waveform has been generated from the mean of ten independent echoes from different permutations of the random statistical surfaces. All parameters are as in Tables II & III except that h_s = 0.

height. Widening the surface height PDF just enhances the power contributions at range bins around the waveform peak. However, the tracking point threshold for a surface with a lognormal PDF reduces by ~5 percentage points (pp) per 10 cm increase in σ_{surf} (Figure 8c). As the lognormal height PDF widens, the mean scattering height of the ice surface falls relative to the maximum height, so that total power contributions from surface facets above the mean height decreases. Relatively lower power has been received at the antenna by the time the transmitted pulse reaches the tracking point. Incidentally, the tracking point is located at an amplitude threshold of 60-80% on the waveform leading edge, for sea ice with lognormal roughness σ_{surf} between 0 and 50 cm, which corresponds to the range of empirical thresholds demonstrating closest association with validation data in [6].

This discrepancy between the shapes of Gaussian and lognormal echoes has important implications for retracking sea ice freeboard from Cryosat-2 waveforms. Leads have negligible roughness, so the range measured to a lead is not influenced by the shape of the height distribution. However, by fitting an echo simulated from a Gaussian surface rather than a lognormal surface to a Cryosat-2 waveform, the measured tracking point from the fit will be overestimated in range and lead to an underestimate of the sea ice surface elevation compared to leads. Figure 9 illustrates how the modelled bias in sea ice freeboard increases nonlinearly as a function of the ice surface roughness height σ_{surf}. By assuming a sea ice density of 915 kg m^{-3} and ocean water density of 1024 kg m^{-3}, we can also estimate the underestimation in ice thickness introduced by this bias. For an ice surface with σ_{surf} = 0.2 m and truly lognormal height distribution, the ice surface elevation will be underestimated by ~5 cm by fitting a Gaussian echo model, translating to an ice thickness error of approximately 0.5 m.

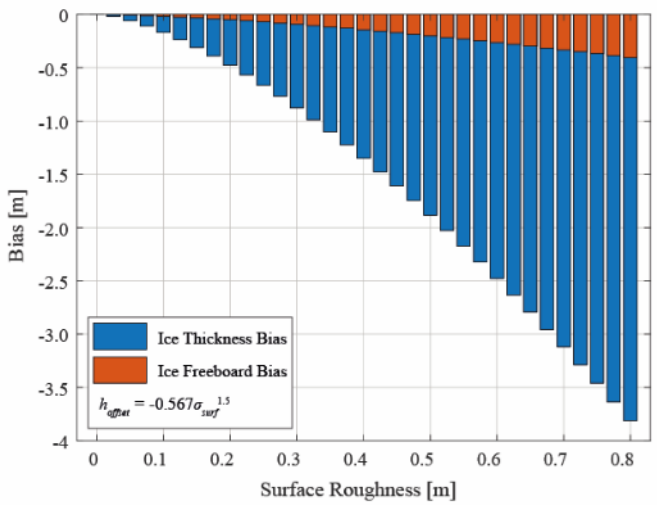

Fig. 9. Modelled underestimation of sea ice freeboard h_{offset}, and approximate ice thickness, as a function of surface roughness height σ_{surf}, when assuming a Gaussian height PDF to model sea ice with truly lognormal surface height statistics.

4) Model Sensitivity to Mixed Surface Types (Leads)

A major question remaining for SAR altimeter measurements of sea ice thickness concerns the separation of echoes from leads versus sea ice, and how leads located outside the nadir position of the antenna contribute to mixed-signal waveforms. Our evaluation of the individual scattering contributions to echoes from snow surface and volume scattering, ice surface scattering and lead surface scattering, allows us to examine this directly. Figure 10 illustrates the scattering contributions from each source when a 50-m wide and 0.2-m deep lead bisects a lognormal sea ice surface parallel to the along-track flight direction. If the lead is at nadir, the offset between t_0 and the tracking point (i.e. the ice freeboard) is a function of lead depth. At 600 m off nadir, scattering from the lead still contributes almost 100% of the backscattered echo, with the waveform having a characteristic specular shape [5]. As the lead moves to 800 and 1000 m off nadir, scattering contributions from the snow surface & volume and especially ice surface increase. The 800-m off-nadir waveform has a characteristic mixed shape comprising quasi-specular and diffuse components. As the lead reaches 1000-m off nadir, it can hardly be detected within the diffuse-type waveform dominated by sea ice surface scattering. At this point scattering from the 20 cm snowpack contributes significantly to the leading-edge of the echo and the tracking point shifts slightly to

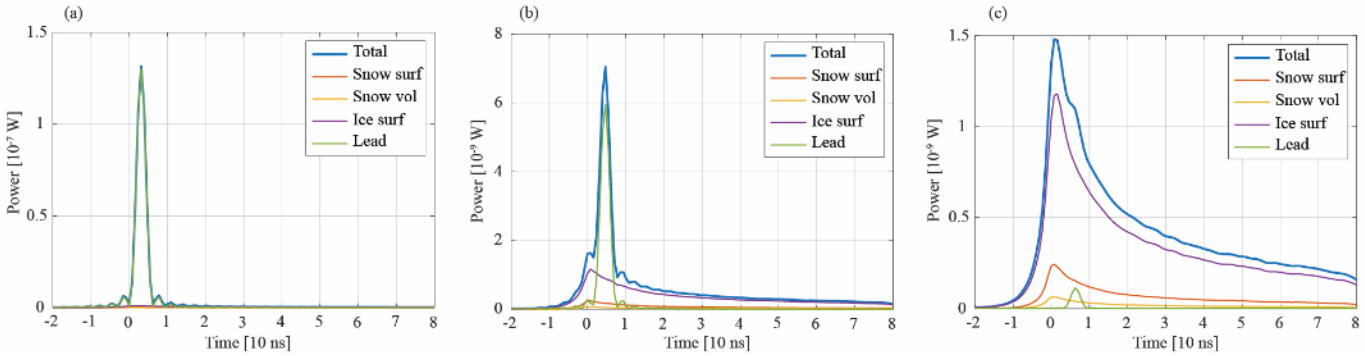

Fig. 10. Total and sub-component echoes derived from the scattering contributions of snow surface roughness, snow volume scattering, ice surface roughness and lead specular reflection, for a lead located (a) 600 m, (b) 800 m and (c) 1000 m off nadir. The lead is 50 m wide and 0.2 m deep, parallel to the along-track satellite velocity vector. The sea ice surface has σ_{surf} = 0.1 m, l_{surf} = 5 m, and h_s = 0.2 m.

an earlier time (Figure 10c). When scattering from the 20-cm deep lead dominates (Figures 10a and b) the primary peak is delayed by several range bins. This correctly identifies the lead elevation, with respect to the ice surface, when the lead is located at nadir, but adds a positive bias to the range when the lead is off nadir [4]. Varying the depth of the lead has little noticeable effect on the shape of the backscattered echo but enhances the ranging bias if the lead is located off nadir.

The relative contributions of each scattering mechanism to the total echo closely depends on the modelled component backscatter (Figure 2). In most cases, sea ice and snow backscatter are well constrained by their physical properties (Table III) and can be modelled reasonably accurately e.g. [14], but the process by which the Ku-band radar wave reflects from a lead is more uncertain. The level of wind-induced roughness has some effect on the power reflected by the lead, see (25). However, the most important yet poorly constrained parameter

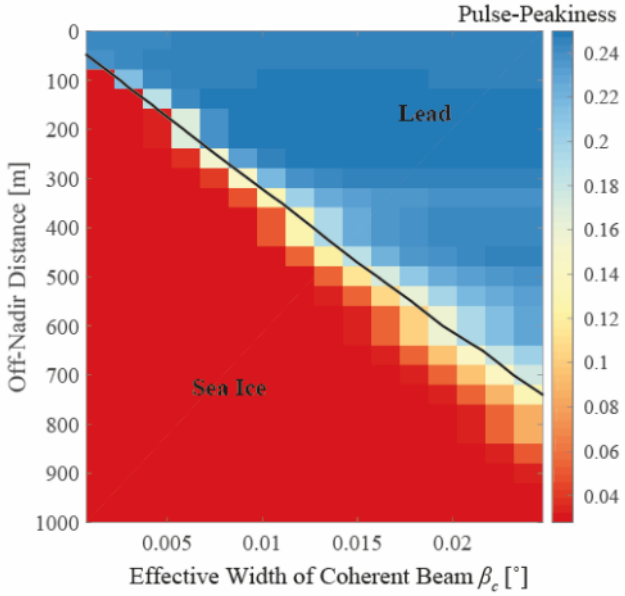

Fig. 11. Impact of the effective angular width of the coherent specular backscatter component β_c and off-nadir lead location, on the pulse-peakiness of a SAR echo waveform. Lead width is 50 m. The black line identifies the pulse-peakiness threshold used by Ricker et al. [6] to separate lead- and sea ice-type waveforms.

is the effective angular width of the coherent backscatter β_c. This parameter has considerable influence on the rate that σ^0_{sw} falls off with θ_{pr}, so controls when the lead can and cannot be 'observed' by the radar at certain look angles. Figure 11 shows the effect of β_c and off-nadir location on the waveform pulse-peakiness for a 50-m lead [56], i.e. when the waveform will and will not be classified as a lead. The threshold proposed by Ricker et al. [6] will still accurately identify a lead 700 m off nadir, if the effective width of the coherent beam is at the wider end. If the coherent beam is at the narrower end ($\beta_c < \frac{\xi_k}{2}$) this threshold will only identify a lead within 350 m off nadir. The lead can clearly be observed over a much greater range of look angles when β_c is larger, leading to a less distinct transition between sea ice- and lead-type waveform shapes as lead off-nadir distance increases.

V. APPLICATION TO SEA ICE OBSERVATIONS

To evaluate how the facet-based altimeter model simulates actual SAR echoes, we use snow-covered sea ice surface topography observations from the Central Arctic Ocean, obtained by the Operation IceBridge (OIB) Airborne Topographic Mapper (ATM) laser scanner on 20th March 2013. The campaign on this date was exceptional because the OIB aircraft flew directly along the track of Cryosat-2 for around 62 km, with the satellite passing over between 3 and 0.2 hours after the underflight. In total the OIB plane passed over the section intersecting Cryosat-2 twelve times, in an elliptical pattern, improving the sampling interval to 0.5-3 m and extending the across-track swath of topography observations to >8 km. We use these observations here to directly compare modelled SAR echoes to real waveforms from Cryosat-2. A detailed description of the method used to merge and georeference the ATM data is provided in the Appendix.

The predominantly multi-year ice along the 62-km OIB section had very a rough surface topography, with σ_{surf} ranging from 0.37 to 0.72 m. A comparison between true and modelled Cryosat-2 echoes from sea ice is shown in Figure 12. The sea ice surface topography (Figure 12a) can be accurately characterized by a lognormal model with fitted σ_{surf} of 0.46 cm (Figure 12b). By simulating backscattered power directly from a triangular mesh of this topography, the numerical echo

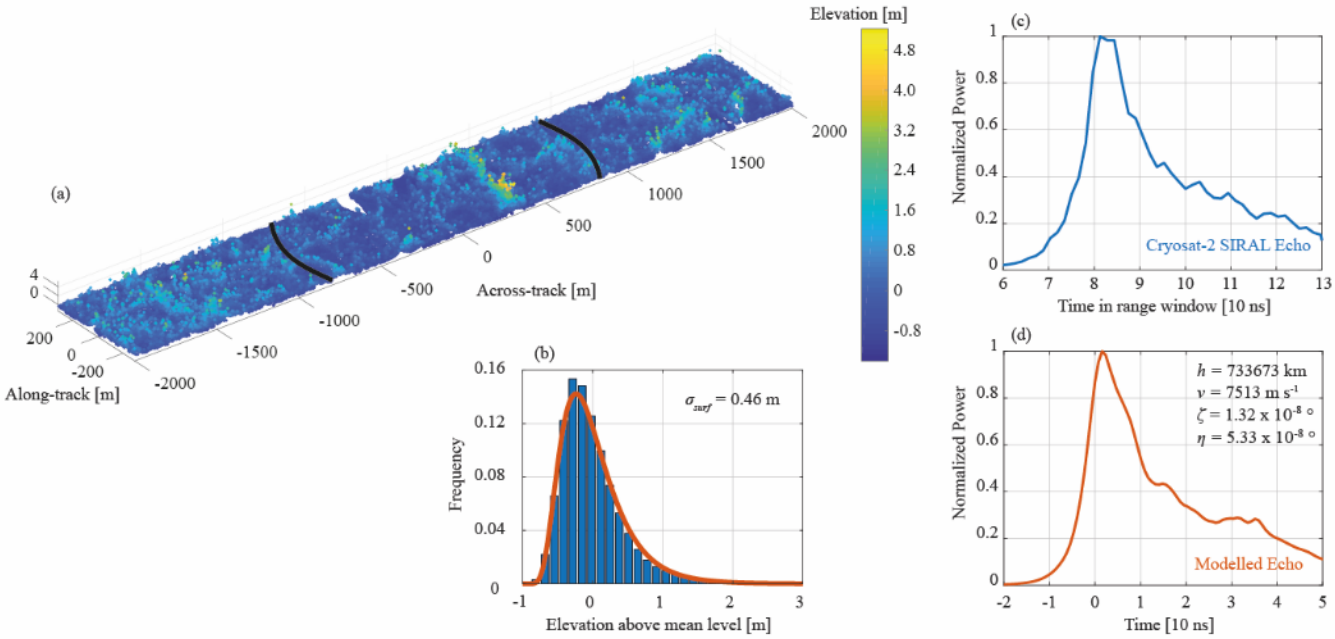

Fig. 12. Example of a Cryosat-2 echo modelled from real sea ice surface topography, including (a) ATM observations of the sea ice surface (with the extent of the pulse-limited footprint in black); (b) a lognormal fit to the surface height PDF; (c) the true Cryosat-2 SIRAL echo, and (d) the modelled echo (using the inset SIRAL antenna parameters).

model can closely characterize the shape of the sea ice waveform leading edge, with a more representative wider and deeper front 'toe' than is common for echoes simulated from surfaces with a Gaussian PDF (Figure 12c and d). The model can also characterize echo trailing-edge power fluctuations, although without the same detail. The discrepancies in this part of the echo are likely caused by spatial heterogeneities in scattering from the snow-covered sea ice that are not captured by the model. The effect of a large (>4 m high) pressure ridge situated ~300 m across-track from nadir (Figure 12a) can be observed in the Cryosat-2 echo, with a slightly stepped leading edge (Figure 12c). The discretization interval of the true Cryosat-2 echo also cuts off the very peak of the waveform (Figure 12d).

A comparison between true and modelled Cryosat-2 echoes from leads intersecting three sea ice floes is shown in Figure 13. The sea ice surface topography (Figure 13a) can once again be accurately characterized by a lognormal model with fitted σ_{surf}

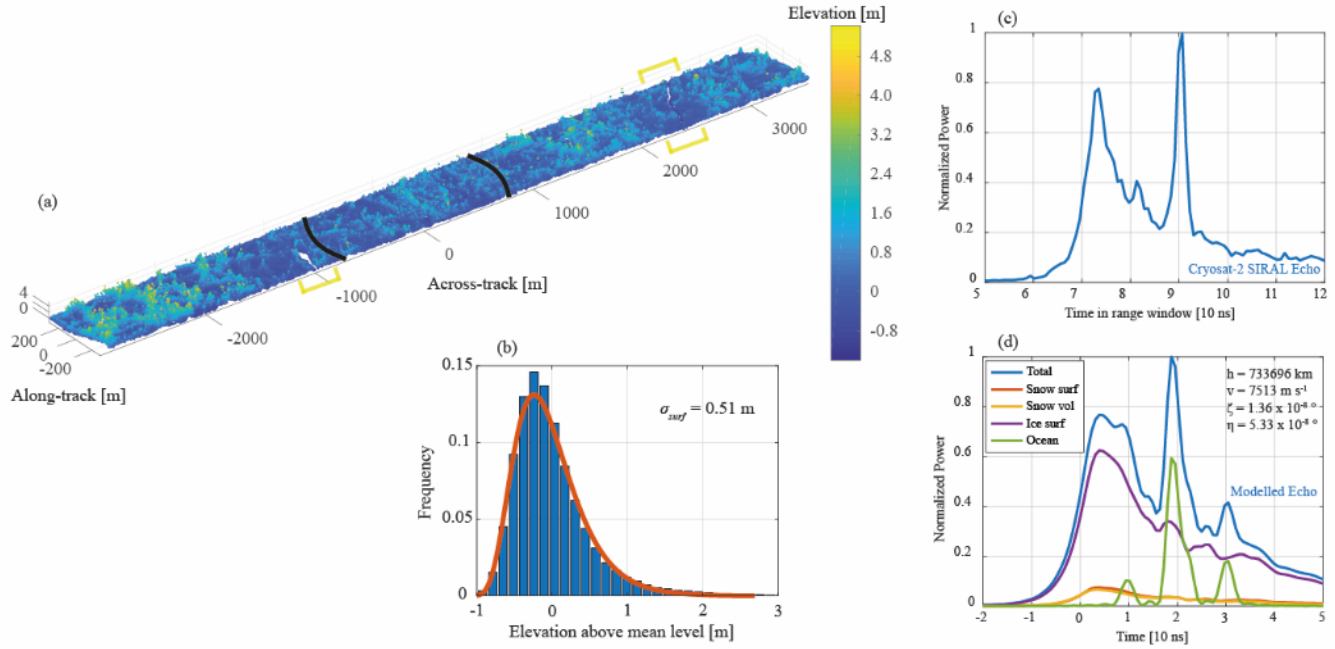

Fig. 13. As in Figure 12, but for a Cryosat-2 echo modelled from leads intersecting three sea ice floes. Lead locations are highlighted in yellow on the point cloud in (a). ATM samples from the leads were classified based on the low intensity of laser reflections.

of 0.51 cm (Figure 13b). When a lead is located close to the nadir point of the footprint, the Cryosat-2 waveform has a strongly-peaked shape indicating dominant specular reflection. We chose this footprint because it represents a case where neither specular nor diffuse scattering dominates, with two thin leads located >1 km from nadir, producing a commonly observed mixed waveform (Figure 13c). Here, we separate the scattering contributions from different surface types within the footprint to examine this integration in detail. Scattering from sea ice around nadir dominates the first peak of the echo (Figure 13d). Very rough pressure ridges beyond the pulse-limited footprint additionally contribute to fluctuations in echo power on the trailing edge. Maximum echo power, however, is produced by specular scattering from the relatively larger lead located at ~2300 m across-track, with the secondary peak occurring approximately 20 ns (3 m in range) after the first. This delay illustrates the potential impact of off-nadir leads on sea ice elevation retrievals, if waveforms are not re-tracked or classified accurately.

Given suitably-detailed topography, the facet-based numerical echo model appears able to closely simulate the complex backscattering response of mixed sea ice/ocean surfaces. Obviously, the number of available coincident Cryosat-2 and high-resolution laser scanning observations is severely limited. However, the comparison between true and simulated Cryosat-2 echoes provides confidence in the model for investigating the sensitivity of waveform shape to physical properties of the sea ice cover, as well as potentially retrieving sea ice properties (freeboard, roughness) through an inversion scheme. A single model run generally takes between 30 and 180 seconds, so curve fitting for property retrievals would require the use of a lookup table, as in e.g. [17].

VI. POTENTIAL APPLICATIONS OF THE FACET-BASED MODEL

Here we have presented the basic architecture and sensitivity of the facet-based model for simulating delay-Doppler SAR echo waveforms from sea ice. There are several avenues for future research that could benefit from using this model.

Past studies have used constant amplitude thresholds on the leading edge to re-track sea ice waveforms, based on early techniques developed for pulse-limited altimetry [5, 6, 18]. However, for SAR altimetry, it has been demonstrated that the true amplitude of the tracking point varies as a function of both primary- and secondary-scale sea ice surface [17]. Here we have shown that the amplitude of the tracking point is also clearly sensitive to the statistical description of the surface roughness. The sea ice surface height distribution is almost always better characterized by a lognormal model instead of the conventionally-used Gaussian model [31]. An obvious research avenue is therefore to evaluate whether SAR echoes modelled from lognormal surfaces provide an improved fit to observed Cryosat-2 waveforms than those from Gaussian surfaces and, if so, whether using a 'lognormal' retracker improves ice thickness retrievals.

A second avenue of study relates to the separation of sea ice and lead classes, and the treatment of mixed-type waveforms. The capability of the facet-based model to separate backscattering contributions from different surfaces within the footprint allows us to assess the probability of an off-nadir lead detection (retracker 'snagging' event) for various scenarios. However, to accurately simulate the echo components, further research is required to understand how backscattering at Ku-band varies between sea ice and ocean, in particular the sensitivity of coherent lead reflection to β_c.

The facet-based model has been flexibly designed to simulate pulse-limited or SAR echoes, at frequencies other than Ku-band. We therefore anticipate that the model could be used to improve retrievals of snow depth on sea ice from dual-altimetry [57, 24, 58]. In theory, at the Ka-band (36 GHz) frequency of the AltiKa satellite, snow surface scattering should dominate and the radar tracking point will be located close to the air-snow interface [24]. Snow depth can be estimated from the difference between AltiKa and Cryosat-2 radar freeboards. However, snow properties [24, 59], sea ice surface roughness [58] and differences between the pulse-limited and SAR-limited footprints [57], can all introduce significant biases into snow depth retrievals if they are not properly accounted for [24, 60]. There have also been clear differences identified between pulse-limited (Envisat) and SAR altimeter (Cryosat-2) returns at Ku-band, likely resulting from sea ice roughness and mixed surface types [61]. For instance, the calibration developed by Lawrence et al. [58] to correct AltiKa and Cryosat-2 radar freeboards to air-snow and snow-ice interfaces, respectively, varies with waveform pulse-peakiness (principally a function of large-scale surface roughness). The facet-based model presented here could be used to directly evaluate the effects of

TABLE IV
MODELLED WAVEFORM SHAPE PARAMETERS FOR VARIOUS SEA ICE SCENARIOS

Scenario[1]	Stack Standard Deviation	Stack Kurtosis	Leading-Edge Width[3]	Pulse Peakiness[4]	Max Echo Power[5]
Nadir Lead[2]	1.3	55.2	0.6	0.48	5.6×10^{-8}
800-m Off-nadir Lead[2]	1.8	44.3	1.5	0.20	8.4×10^{-10}
900-m Off-nadir Lead[2]	6.1	6.2	2.4	0.08	2.2×10^{-11}
1000-m Off-nadir Lead[2]	12.8	2.6	2.8	0.06	1.0×10^{-11}
Sea Ice Roughness $\sigma = 5$ cm	15.6	1.6	2.6	0.06	1.2×10^{-11}
Sea Ice Roughness $\sigma = 10$ cm	16.0	1.5	2.7	0.06	1.1×10^{-11}
Sea Ice Roughness $\sigma = 20$ cm	17.6	1.5	2.8	0.06	9.4×10^{-12}
Sea Ice Roughness $\sigma = 50$ cm	19.3	1.5	3.3	0.06	5.7×10^{-12}

[1] All model runs performed with the reference parameters sets in Tables II and III, lognormal large-scale roughness of 10 cm, and a snow depth of zero. [2] For a reference lead width of 50 m and depth of 0.2 m, as in Figure 10. [3] Waveform leading-edge definition taken from Paul et al. [61]. [4] Waveform pulse peakiness definition taken from Kurtz et al. [17]. [5] Estimated, in Watts, but without atmospheric transmission, snow or other losses.

surface roughness and snow properties on the expected waveform shape, including pulse-peakiness, of both AltiKa and Cryosat-2. Theoretical corrections obtained from these simulation results could improve the empirical corrections already developed.

Rather than using delay-Doppler SAR processing, as described here, the facet-based model could be readily converted to exploit the fully-focused SAR altimetry processing of [62], which is an avenue of huge potential. This could be valuable for understanding the sensitivity of the along-track SAR focused echo to sea ice surfaces with heterogenous scatterers and complex topography.

Finally, the facet-based model could be extended to simulate the echo cross-product for an interferometric radar altimeter like Cryosat-2. This would involve calculating the cross-product impulse responses of the surface at the interferometer baseline, as in e.g. [28], providing simulations for the coherence and phase of the echo cross-product for a given snow-covered ice surface. A particularly valuable application of this could be for understanding the sensitivity of the radar echo cross-product to the slope, roughness, melting state and backscattering properties of glacial ice [63, 64]. OIB underflights of Cryosat-2 tracks over ice sheets could, as here, provide a means of validating simulations results.

VII. Conclusion

Although Cryosat-2 has provided measurements of Arctic sea ice thickness at unprecedented resolution and accuracy since 2010, several areas of uncertainty remain – principally concerning the sensitivity of the backscattered echo to snow properties, sea ice surface roughness and mixed surface types. In this paper we have presented a novel facet-based numerical model of the delay-Doppler synthetic aperture radar altimeter echo from snow-covered sea ice. The model can simulate echoes from a triangular-mesh of real sea ice topography, obtained from airborne laser scanning data, or from virtual sea ice surfaces generated by statistical models of the ice surface roughness. Backscattering from the air-snow interface, snow volume, snow-ice interface and leads are simulated directly from the Integral Equation Model and Mie particle scattering theory. This allows us to partition the relative contributions of each scattering mechanism to the final power echo.

We have demonstrated that the backscattered multi-looked echo from sea ice varies weakly as a function of radar antenna properties (e.g. pitch and roll). The modelled echo for a sea ice surface with Gaussian topography compares closely to the analogous echo simulated by SAMOSA+ analytical waveform model for a rough Gaussian ocean surface. However, airborne laser scanner observations (including those presented here) have shown that sea ice surface roughness is typically better characterized by a lognormal height distribution than a Gaussian one. Indeed, echoes simulated from OIB laser scanner observations of lognormal sea ice in the Central Arctic Ocean compare well to coincident Cryosat-2 SAR-mode waveforms. By assuming Gaussian height statistics for truly lognormal sea ice surfaces, the tracking point (and thus ice freeboard) will be underestimated by ~5 cm for sea ice with rms roughness height of 0.2 m. This translates to an ice thickness underestimation of around 50 cm. The tracking point for echoes from lognormal surfaces varies nonlinearly as a function of roughness; however, for sea ice surfaces with typical roughness, the tracking threshold is between 60 and 80% of the leading-edge power.

A set of modelled waveform shape parameters, for different sea ice surface roughness and lead scenarios, are shown in Table IV. Shape parameters vary within the typical ranges presented in previous studies e.g. [5, 6, 13, 17, 56]; however, the values in Table IV provide guidance for detailed interpretation of echoes based on their shape. These model scenarios can improve the discrimination between echoes from sea ice versus leads.

We anticipate that the facet-based SAR echo model will prove to be a valuable tool for investigating the sensitivity of backscattered waveforms to a variety of sea ice properties: surface roughness, off-nadir lead detection, snow depth at various radar frequencies, and potentially glacier ice properties. Our future work will aim to utilize this model in an inversion scheme to retrieve key sea ice properties from Cryosat-2 and other SAR altimeters.

Appendix

Airborne Topographic Mapper (ATM) observations from OIB on 20th March 2013 were processed using the following methodology. A scanner-azimuth-dependent bias was removed from all point clouds along the 62-km section coincident to the Cryosat-2 overpass, following [65]. The Level 1b ATM data have a precision of 0.03-0.05 m, a typical sampling interval on-the-ground of 4-12 m, and single-track swath width of ~600 m [65]. However, on this date the OIB plane passed over the 62-km section intersecting Cryosat-2 twelve times, in an elliptical pattern, to improve the sampling interval (where tracks intersected) to 0.5-3 m and extend the across-track swath of topography observations to >8 km. The along-track footprint of SIRAL is limited to ~300 m through SAR processing. The across-track pulse-limited footprint is ~1500 m, though the trailing-edge of the echo can include backscattered power above the noise floor from surface facets located >5000 m away from nadir. Thus, to characterize as much of the echo as possible, we generated a merged point cloud from all twelve ATM tracks. This was aligned to the Cryosat-2 overflight to identify 207 independent sea ice/lead elevation models, of approximately 500 by 8000 m size, intersecting individual Cryosat-2 footprints. Each of these elevation models was finally converted, at full resolution, into a triangular mesh of facets for use in the numerical echo model and compared to the true Cryosat-2 received waveforms.

As is typical, the ice floes in the Central Arctic Ocean region were drifting over the three-hour period that ATM observations were acquired, so the process of merging individual tracks was not straightforward. The final ATM track was flown at UTM 17:16, twelve minutes before the Cryosat-2 overpass, so all point clouds were georeferenced to the location of this track. General motion of the region's icepack was determined by accurately registering sets of aerial photographs from the OIB Digital Mapping System (DMS) at the centre and each end of the coincident 62 km section. Over the 3-hr measurement period the icepack drifted at 0.7 km hr^{-1} to the North-northwest,

with little internal deformation. Starting from the track immediately adjacent to the reference track, each point cloud was displaced in the direction opposing the ice drift by 0.7 km hr^{-1} multiplied by the time offset between measurements. The *MATLAB* iterative closest point (ICP) algorithm was then used to tune the point cloud-to-point cloud registration by minimizing the rms distance between pairs of points from overlapping regions, with the vertical fit between points weighted twice as heavily as the horizontal fit. Each point in a pair will rarely come from the same location, so RMSE between pairs will never be zero; however, including the ICP algorithm registration step was critical and improved the overall fit by around 300%. The region of interest included several leads and cracks which could be aligned and used to verify the quality of the final merged point cloud, although understandably the fit is imperfect and could have introduced artificial facets into the sea ice models. Maps of the twelve point clouds before and after they were merged and georeferenced are shown in Figure 14.

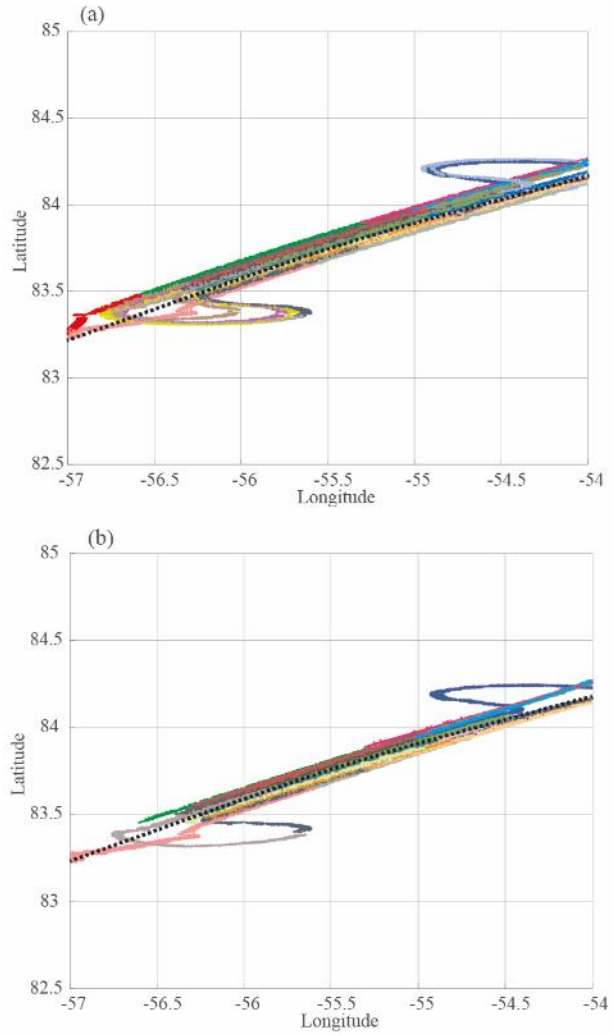

Fig. 14. Maps of the twelve Airborne Topographic Mapper sections intersecting a Cryosat-2 overpass from the Operation IceBridge campaign on 20th March 2013, (a) before and (b) after the point clouds were merged and georeferenced. The maximum degrees of arc a point cloud was translated corresponded to approximately 0.02° and the location of the Cryosat-2 overpass is given by the dashed black lines.

Normally the OIB aircraft records estimates for the snow depth on sea ice from the *CReSIS* Frequency-Modulated Continuous Wave (FMCW) snow radar alongside the ATM topography measurements. However, the snow radar was not operational for the 20th March 2013 campaign because the flight altitude was increased to widen the ATM swath. So here we simply simulate Cryosat-2 waveforms assuming the upper 20 cm of the ATM topography is snow [66]. All other snow properties are kept as in Table III.

REFERENCES

[1] M. McMillan, A. Shepherd, A. Sundal, K. Briggs, A. Muir, A. Ridout, A. Hogg and D. Wingham, "Increased ice losses from Antarctica detected by CryoSat-2," *Geophys. Res. Lett.*, vol. 41, no. 11, pp. 3899-3905, 2014.

[2] D. Sandwell, E. Garcia, K. Soofi, P. Wessel, M. Chandler and W. Smith, "Toward 1-mGal accuracy in global marine gravity from CryoSat-2, Envisat, and Jason-1," *The Leading Edge*, vol. 32, no. 8, pp. 892-899, 2013.

[3] A. Abulaitijiang, O. Andersen and L. Stenseng, "Coastal sea level from inland CryoSat-2 interferometric SAR altimetry," *Geophys. Res. Lett.*, vol. 42, no. 6, pp. 1841-1847, 2015.

[4] T. Armitage, S. Bacon and R. Kwok, "Arctic sea level and surface circulation response to the Arctic Oscillation," *Geophys. Res. Lett.*, vol. 45, no. 13, pp. 6576-6584, 2018.

[5] S. Laxon, K. Giles, A. Ridout, D. Wingham, R. Willat, R. Cullen, R. Kwok, A. Schweiger, J. Zhang, C. Haas, S. Hendricks, R. Krishfield, N. Kurtz, S. Farrell and M. Davidson, "CryoSat-2 estimates of Arctic sea ice thickness and volume," *Geophys. Res. Lett.*, vol. 40, pp. 732-737, 2013.

[6] R. Ricker, S. Hendricks, V. Helm, H. Skourup and M. Davidson, "Sensitivity of CryoSat-2 Arctic sea-ice freeboard and thickness on radar-waveform interpretation," *Cryosphere*, vol. 8, pp. 1607-1622, 2014.

[7] V. Guemas, E. Blanchard-Wrigglesworth, M. Chevallier, J. Day, M. Déqué, F. Doblas-Reyes, N. Fučkar, A. Germe, E. Hawkins, S. Keeley and T. Koenigk, "A review on Arctic sea-ice predictability and prediction on seasonal to decadal time-scales," *Quat. J. Royal Met. Soc.*, vol. 142, no. 695, pp. 546-561, 2016.

[8] R. Allard, S. Farrell, D. Hebert, W. Johnston, L. Li, N. Kurtz, M. Phelps, P. Posey, R. Tilling, A. Ridout and A. Wallcraft, "Utilizing CryoSat-2 Sea Ice Thickness to Initialize a Coupled Ice-Ocean Modeling System," *Adv. Space Res.*, vol. In Press, 2018.

[9] J. Stroeve, D. Schroder, M. Tsamados and D. Feltham, "Warm winter, thin ice?," *Cryosphere*, vol. 12, no. 5, pp. 1791-1809, 2018.

[10] D. Schröder, D. L. Feltham, M. Tsamados, A. Ridout and R. Tilling, "New insight from CryoSat-2 sea ice thickness for sea ice modelling," *Cryosphere Discuss.*, vol. In Review, 2018.

[11] D. Wingham, C. Francis, S. Baker, C. Bouzinac, D. Brockley, R. Cullen, P. de Chateau-Thierry, S. Laxon, U. Mallow, C. Mavrocordatos and L. Phalippou, "CryoSat: A mission to determine the fluctuations in Earth's land and marine ice fields," *Adv. Space Res.*, vol. 37, no. 4, pp. 841-871, 2006.

[12] G. D. Quartly, E. Rinne, M. Passaro, O. B. Andersen, D. S. S. Fleury, K. Guerreiro, A. Guillot, S. Hendricks, A. A. Kurekin, F. L. Müller, R. Ricker, H. Skourup and M. Tsamados, "Review of Radar Altimetry Techniques over the Arctic Ocean: Recent Progress and Future Opportunities for Sea Level and Sea Ice Research," *Cryospher Discuss.*, 2018.

[13] R. Kwok and G. Cunningham, "Variability of Arctic sea ice thickness and volume from Cryosat-2," *Phil. Trans. R. Soc. A*, vol. 373, no. 20140157, 2015.

[14] A. Komarov, J. Landy, S. Komarov and D. Barber, "Evaluating Scattering Contributions to C-Band Radar Backscatter From Snow-Covered First-Year Sea Ice at the Winter–Spring Transition Through Measurement and Modeling," *IEEE Trans. Geosci. Rem. Sens.*, vol. 55, no. 10, pp. 5702-5718, 2017.

[15] N. Firoozy, P. Majobai, J. Landy and D. Barber, "Landfast First-Year Snow-Covered Sea Ice Reconstruction via Electromagnetic Inversion," *IEEE J. Select. Topics Appl. Earth Obs. Rem. Sens.*, vol. 9, no. 6, pp. 2414-2428, 2015.

[16] T. Armitage and M. Davidson, "Using the Interferometric Capabilities of the ESA Cryosat-2 Mission to Improve the Accuracy of Sea Ice Freeboard Retrievals," *IEEE Trans. Geosci. Rem. Sens.*, vol. 52, no. 1, pp. 529-536, 2013.

[17] N. Kurtz, N. Galin and M. Studinger, "An improved CryoSat-2 sea ice freeboard retrieval algorithm through the use of waveform fitting," *Cryosphere*, vol. 8, pp. 1217-1237, 2014.

[18] R. L. Tilling, A. Ridout and A. Shepherd, "Near-real-time Arctic sea ice thickness and volume from CryoSat-2," *Cryosphere*, vol. 10, pp. 2003-2012, 2016.

[19] F. Ulaby, R. Moore and A. Fung, Microwave Remote Sensing: Active and Passive, vol. II, Boston, MA: Artech House, 1982.

[20] R. L. Tilling, A. Ridout and A. Shepherd, "Estimating Arctic sea ice thickness and volume using CryoSat-2 radar altimeter data," *Adv. Space Sci.*, vol. 62, no. 6, pp. 1203-1225, 2018.

[21] A. Wernecke and L. Kaleschke, "Lead detection in Arctic sea ice from CryoSat-2: quality assessment, lead area fraction and width distribution," *Cryosphere*, vol. 9, no. 5, pp. 1955-1968, 2015.

[22] J. Landy, D. Isleifson, A. Komarov and D. Barber, "Parameterization of centimeter-scale sea ice surface roughness using terrestrial LiDAR," *IEEE Trans. Geosci. Rem Sens.*, vol. 53, no. 3, pp. 1271-1286, 2015.

[23] S. Dinardo, L. Fenoglio-Marc, C. Buchhaupt, M. Becker, R. Scharroo, M. Fernandes and J. Benveniste, "Coastal SAR and PLRM altimetry in german bight and west baltic sea," *Adv. Space Sci.*, vol. In Press, 2017.

[24] K. Guerreiro, S. Fleury, E. Zakharova, F. Rémy and A. Kouraev, "Potential for estimation of snow depth on Arctic sea ice from CryoSat-2 and SARAL/AltiKa missions," *Rem. Sens. Env.*, vol. 186, pp. 339-349, 2016.

[25] R. Willatt, S. Laxon, K. Giles, R. Cullen, C. Haas and V. Helm, "Ku-band radar penetration into snow cover on Arctic sea ice using airborne data," *Ann. Glaciol.*, vol. 52, no. 57, pp. 197-205, 2011.

[26] V. Nandan, T. Geldsetzer, J. Yackel, M. Mahmud, R. Scharien, S. Howell, J. King, R. Ricker and B. Else, "Effect of snow salinity on CryoSat-2 Arctic first-year sea ice freeboard measurements," *Geophys. Res. Lett.*, vol. 44, no. 20, pp. 10419-10426, 2017.

[27] C. Ray, C. Martin-Puig, M. Clarizia, G. Ruffini, S. Dinardo, C. Gommenginger and J. Benveniste, "SAR altimeter backscattered waveform model," *IEEE Trans. Geosci. Rem. Sens.*, vol. 53, no. 2, pp. 911-919, 2015.

[28] D. Wingham, K. Giles, N. Galin, R. Cullen, T. Armitage and W. Smith, "A Semianalytical Model of the Synthetic Aperture, Interferometric Radar Altimeter Mean Echo, and Echo Cross-Product and Its Statistical Fluctuations," *IEEE Trans. Geosci. Rem. Sens.*, vol. 56, no. 5, pp. 2539-2553, 2018.

[29] R. Arthern, D. Wingham and A. Ridout, "Controls on ERS altimeter measurements over ice sheets: Footprint-scale topography, backscatter fluctuations, and the dependence of microwave penetration depth on satellite orientation," *J. Geophys. Res. Atmos.*, vol. 106, no. D24, pp. 33471-33484, 2001.

[30] C. Buchhaupt, L. Fenoglio-Marc, S. Dinardo, R. Scharroo and M. Becker, "A fast convolution based waveform model for conventional and unfocused SAR altimetry," *Adv. Space Res.*, vol. 62, no. 6, pp. 1445-1463, 2018.

[31] M. Rivas, J. Maslanik, J. Sonntag and P. Axelrad, "Sea Ice Roughness From Airborne LIDAR Profiles," *IEEE Trans. Geosci. Rems. Sens.*, vol. 44, no. 11, pp. 3032-3037, 2006.

[32] M. Leppäranta, The drift of sea ice, Berlin: Springer Science & Business Media, 2011.

[33] C. Liu, J. Chao, W. Gu, L. Li and Y. Xu, "On the surface roughness characteristics of the land fast sea-ice in the Bohai Sea," *Acta Oceanol. Sin.*, vol. 33, no. 7, pp. 97-106, 2014.

[34] J. F. Beckers, A. Renner, G. Spreen, S. Gerland and C. Haas, "Sea-ice surface roughness estimates from airborne laser scanner and laser altimeter observations in Fram Strait and north of Svalbard," *Ann. Glaciol.*, vol. 56, pp. 235-244, 2015.

[35] G. Timco and R. Burden, "An analysis of the shapes of sea ice ridges," *Cold Reg. Sci. Tech.*, vol. 25, no. 1, pp. 65-77, 1997.

[36] S. Nasonova, R. Scharien, C. Haas and S. Howell, "Linking Regional Winter Sea Ice Thickness and Surface

Roughness to Spring Melt Pond Fraction on Landfast Arctic Sea Ice," *Rem. Sens.*, vol. 10, no. 1, p. 37, 2017.

[37] P. Wadhams and T. Davy, "On the spacing and draft distributions for pressure ridge keels," *J. Geophys. Res. Oceans*, vol. 91, no. C9, pp. 10697-10708, 1986.

[38] G. Brown, "The average impulse response of a rough surface and its applications," *IEEE Trans. Antenna Prop.*, vol. 25, no. 1, pp. 67-74, 1977.

[39] T. Hagfors, "Remote probing of the moon by infrared and microwave emissions and by radar," *Radio Sci.*, vol. 5, no. 2, pp. 189-277, 1970.

[40] J. Landy, A. Komarov and D. Barber, "Numerical and experimental evaluation of terrestrial LiDAR for parameterizing centimeter-scale sea ice surface roughness," *IEEE Trans. Geosci. Rem. Sens.*, vol. 53, no. 9, pp. 4887-4898, 2015.

[41] B. Hughes, "On the use of lognormal statistics to simulate one-and two-dimensional under-ice draft profiles," *J. Geophys. Res. Oceans*, vol. 96, no. C12, pp. 22101-22111, 1991.

[42] T. Jacobs, T. Junge and L. Pastewka, "Quantitative characterization of surface topography using spectral analysis," *Surf. Topo. Metrol. Prop.*, vol. 5, no. 1, p. 13001, 2017.

[43] K. Giles, S. Laxon, D. Wingham, D. Wallis, W. Krabill, C. Leuschen, D. McAdoo, S. Manizade and R. Raney, "Combined airborne laser and radar altimeter measurements over the Fram Strait in May 2002," *Rem. Sens. Env.*, vol. 111, no. 2, pp. 182-194, 2007.

[44] M. Makynen and M. Hallikainen, "Simulation of ASIRAS altimeter echoes for snow-covered first-year sea ice," *IEEE Geosci. Rem. Sens. Lett.*, vol. 6, no. 3, pp. 486-490, 2009.

[45] D. Wingham and D. Wallis, "The rough surface impulse response of a pulse-limited altimeter with an elliptical antenna pattern," *IEEE Antenna Wireless Prop. Lett.*, vol. 9, pp. 232-235, 2010.

[46] M. Hallikainen and D. Winebrenner, "The Physical Basis for Sea Ice Remote Sensing," in *Microwave Remote Sensing of Sea Ice*, F. Carsey, Ed., Washington DC, American Geophysical Union Monograph Series, 1992, pp. 30-46.

[47] D. Winebrenner and e. a. , "Microwave Sea Ice Signature Modeling," in *Microwave Remote Sensing of Sea Ice*, vol. 68, F. Carsey, Ed., Washington, DC, American Geophysical Union, 1992, pp. 137-175.

[48] A. K. Fung, Microwave Scattering and Emission Models and Their Applications, Artech House, Inc., 1994.

[49] A. Fung and K. Chen, "An update on the IEM surface backscattering model," *IEEE Geosci. Rem. Sens. Lett.*, vol. 1, no. 2, pp. 75-77, 2004.

[50] C. Mätzler, Thermal microwave radiation: applications for remote sensing, vol. 52, Stevenage: Institution of Engineering and Technology, 2006.

[51] A. Stogryn, "Equations for calculating the dielectric constant of saline water," *IEEE Trans. Micr. Theory Tech.*, vol. 19, no. 8, pp. 733-736, 1971.

[52] G. Cox and W. Weeks, "Equations for determining the gas and brine volumes in sea-ice samples," *J. Glaciol.*, vol. 29, no. 102, pp. 306-316, 1983.

[53] A. Fung and H. Eom, "Coherent scattering of a spherical wave from an irregular surface," *IEEE Trans. Geosci. Rem. Sens.*, vol. 31, no. 1, pp. 68-72, 1983.

[54] W. Dierking, "RMS slope of exponentially correlated surface roughness for radar applications," *IEEE Trans. Geosci. Rem. Sens.*, vol. 38, no. 3, pp. 1451-1454, 2000.

[55] N. Galin, D. Wingham, R. Cullen, M. Fornari, W. Smith and S. Abdalla, "Calibration of the CryoSat-2 interferometer and measurement of across-track ocean slope," *IEEE Trans. Geosci. Rem. Sens.*, vol. 51, no. 1, pp. 57-72, 2013.

[56] J. Landy, D. Babb, J. Ehn, N. Theriault and D. Barber, "Sea ice thickness in the Eastern Canadian Arctic: Hudson Bay Complex & Baffin Bay," *Rem. Sens. Env.*, vol. 200, pp. 281-294, 2017.

[57] T. Armitage and A. Ridout, "Arctic sea ice freeboard from AltiKa and comparison with CryoSat-2 and Operation IceBridge," *Geophys. Res. Lett.*, vol. 42, no. 16, pp. 6724-6731, 2015.

[58] I. Lawrence, M. Tsamados, J. Stroeve, T. Armitage and A. Ridout, "Estimating snow depth over Arctic sea ice from calibrated dual-frequency radar freeboards," *Cryosphere Discuss.*, 2018.

[59] R. Kwok, "Simulated effects of a snow layer on retrieval of CryoSat-2 sea ice freeboard," *Geophys. Res. Lett.*, vol. 41, pp. 5014-5020, 2014.

[60] K. Guerreiro, S. Fleury, E. Zakharova, A. Kouraev, F. Rémy and P. Maisongrande, "Comparison of CryoSat-2 and ENVISAT radar freeboard over Arctic sea ice: toward an improved Envisat freeboard retrieval," *Cryosphere*, vol. 11, no. 5, pp. 2059-2073, 2017.

[61] S. Paul, S. Hendricks, R. Ricker, S. Kern and E. Rinne, "Empirical parametrization of Envisat freeboard retrieval of Arctic and Antarctic sea ice based on CryoSat-2: progress in the ESA Climate Change Initiative," *Cryosphere*, vol. 12, no. 7, pp. 2437-2460, 2018.

[62] A. Egido and W. Smith, "Fully Focused SAR Altimetry: Theory and Applications," *IEEE Trans. Geosci. Rem. Sens.*, vol. 55, no. 1, pp. 392-406, 2017.

[63] L. Gray, D. Burgess, L. Copland, R. Cullen, N. Galin, R. Hawley and V. Helm, "Interferometric swath processing of Cryosat data for glacial ice topography," *Cryosphere*, vol. 7, no. 6, pp. 1857-1867, 2013.

[64] J. Nilsson, P. Vallelonga, S. Simonsen, L. Sørensen, R. Forsberg, D. Dahl-Jensen, M. Hirabayashi, K. Goto-Azuma, C. Hvidberg, H. Kjær and K. Satow, "Greenland 2012 melt event effects on CryoSat-2 radar altimetry," *Geophys. Res. Lett.*, vol. 42, no. 10, pp. 3919-3926, 2015.

[65] D. Yi, J. Harbeck, S. Manizade, N. Kurtz, M. Studinger and M. Hofton, "Arctic Sea Ice Freeboard Retrieval With

Waveform Characteristics for NASA's Airborne Topographic Mapper (ATM) and Land, Vegetation, and Ice Sensor (LVIS)," *IEEE Trans. Geosci. Rem. Sens.*, vol. 53, no. 3, pp. 1403-1410, 2015.

[66] M. Webster, I. Rigor, S. Nghiem, N. Kurtz, S. Farrell, D. Perovich and M. Sturm, "Interdecadal changes in snow depth on Arctic sea ice," *J. Geophys. Res. Oceans*, vol. 119, pp. 5395-5406, 2014.

[67] R. G. Onstott, "5. SAR and Scatterometer Signatures of Sea Ice," in *Microwave Remote Sensing of Sea Ice*, F. D. Carsey, Ed., American Geophysical Union, 1992, pp. 73-104.

[68] C. Petrich and H. Eicken, "Growth, Structure and Properties of Sea Ice," in *Sea Ice*, Oxford, Blackwell Publishing Ltd, 2010, pp. 23-78.

[69] M. Sturm, J. Holmgren and D. Perovich, "Winter snow cover on the sea ice of the Arctic Ocean at the Surface Heat Budget of the Arctic Ocean (SHEBA): Temporal evolution and spatial variability," *J. Geophys. Res. Oceans*, vol. 107, no. C10, 2002.

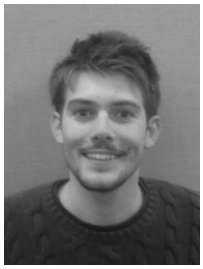

Jack C. Landy (M'14-16) received the B.Sc. (Hons.) degree in physical geography from the University of Durham, U.K., in 2009 and the M.Sc. (Hons.) degree in remote sensing from the University of Durham in 2011. He received the Ph.D. degree from the University of Manitoba, Canada, in 2016, specializing in sea ice geophysics and remote sensing, before joining the Bristol Glaciology Centre, University of Bristol, U.K., as Lecturer in Geodesy.

Dr. Landy's primary research interest is in developing optical and microwave remote sensing methods for monitoring the physical properties of Arctic sea ice. He has used terrestrial and airborne Light Detection and Ranging (LiDAR), as well as satellite laser and radar altimetry, to study the multi-scale properties of sea ice surface roughness and understand the physical processes of sea ice melt. He has participated in more than 45 weeks of field-based research on sea ice in the Canadian sector of the Arctic.

Michel Tsamados holds the prestigious Agrégation de physique (2004), received his M.S. (2005) in statistical physics from l'École Normale Supérieure de Lyon, and his Ph.D. (2009) in theoretical physics at Université Claude Bernard where he studied the mechanical response of glassy materials from a theoretical and modelling perspective. After receiving his Ph.D., Michel held several postdoctoral positions at the Centre for Polar Observations and Modelling at UCL and Reading Universities where he implemented several new sea ice model parameterizations including a new anisotropic rheology and a new form drag formulation into the Los Alamos CICE sea ice model.

Since 2014, Michel has been a lecturer in the Department of Earth Sciences and has contributed to the development and analysis of several satellite products in the polar regions ranging from sea ice thickness, sea surface elevation, significant wave heights, snow on sea ice, sea ice roughness, melt pond concentration, etc. He currently leads the working group on data science for climate and the environment at the Alan Turing Institute and sits on the mission advisory group for the Earth Explorer 9 ESA mission Sea surface KInematics Multiscale monitoring satellite (SKIM).

Randall K. Scharien received the Bachelor's (Hons.) degree from the University of Manitoba, Winnipeg, MB, Canada in 2000, and Masters and Ph.D. degrees in microwave remote sensing of sea ice from the University of Calgary, Calgary, AB, Canada in 2004 and 2010, respectively. He was a European Space Agency Changing Earth Science Network investigator from 2013 to 2014, before being appointed to a faculty position in remote sensing at the Department of Geography, University of Victoria, Victoria, BC, Canada in 2014. His research interests include microwave remote sensing, synthetic aperture radar, and atmosphere-ice-ocean exchange processes.